**Weierstraß-Institut**
**für Angewandte Analysis und Stochastik**

**Leibniz-Institut im Forschungsverbund Berlin e. V.**

Preprint ISSN 2198-5855

# Generalized Poisson-Nernst-Planck-based physical model of $O_2$|LSM|YSZ electrode

Vojtěch Miloš[1,2], Petr Vágner[3], Daniel Budáč[1], Michal Carda[1], Martin Paidar[1],

Jürgen Fuhrmann[3], Karel Bouzek[1]

submitted: December 16, 2020

[1] Department of Inorganic Technology
University of Chemistry and Technology
Technická 5
166 28 Praha 6, Czech Republic
E-Mail: vojtech.milos@vscht.cz
daniel.budac@vscht.cz
michal.carda@vscht.cz
martin.paidar@vscht.cz
karel.bouzek@vscht.cz

[2] Faculty of Mathematics and Physics
Charles University
Sokolovská 49/83
186 75 Praha 8, Czech Republic

[3] Weierstrass Institute
Mohrenstr. 39
10117 Berlin
Germany
E-Mail: petr.vagner@wias-berlin.de
juergen.fuhrmann@wias-berlin.de

No. 2797
Berlin 2020

2010 *Mathematics Subject Classification.* 65N30 78A57 80A17.

*Key words and phrases.* Solid oxide cells, charge layer, thermodynamics, electrode potential.

This work was supported by the German Research Foundation, DFG project no. FU 316/14-1, and by the Czech Science Foundation, GAČR project no. 19-14244J. VM gratefully acknowledge support by the student project in Mathematical and computer modeling and Didactics of Physics no. SVV-2020-260577.

Edited by
Weierstraß-Institut für Angewandte Analysis und Stochastik (WIAS)
Leibniz-Institut im Forschungsverbund Berlin e. V.
Mohrenstraße 39
10117 Berlin
Germany

Fax: +49 30 20372-303
E-Mail: preprint@wias-berlin.de
World Wide Web: http://www.wias-berlin.de/

# Generalized Poisson-Nernst-Planck-based physical model of $O_2$|LSM|YSZ electrode

V. Miloš, P. Vágner, D. Budáč, M. Carda, M. Paidar, J. Fuhrmann, K. Bouzek

**Abstract**

The paper presents a generalized Poisson-Nernst-Planck model of an yttria-stabilized zirconia electrolyte developed from first principles of nonequilibrium thermodynamics which allows for spatial resolution of the space charge layer. It takes into account limitations in oxide ion concentrations due to the limited availability of oxygen vacancies. The electrolyte model is coupled with a reaction kinetic model describing the triple phase boundary with electron conducting lanthanum strontium manganite and gaseous phase oxygen. By comparing the outcome of numerical simulations based on different formulations of the kinetic equations with results of EIS and CV measurements we attempt to discern the existence of separate surface lattice sites for oxygen adatoms and $O^{2-}$ from the assumption of shared ones. Furthermore, we discern mass-action kinetics models from exponential kinetics models.

## 1 Introduction

Solid oxide cells (SOC) constitute an important segment of the currently developed system of hydrogen technologies designated for more effective utilization of energy resources and reduction of the carbon dioxide emissions. Solid oxide cells operate at temperatures above 600 °C posing limitations on the available techniques for experimental investigation, in particular in-situ methods. Mathematical models of SOC have the potential to enable a spatially resolved interpretation of current-voltage measurements and their translation into information about e.g. the kinetic rates or the profile of the electrostatic potential.

The electrolyte material of choice for the present investigation Yttria-stabilized Zirconia (YSZ). The $Y^{3+}$ ions occupy the $Zr^{4+}$ lattice sites and thus introduce the $O^{2-}$ vacancies,

$$\mathrm{Y_2\,O_3} \xrightarrow{\mathrm{ZrO_2}} 2\,\mathrm{Y'_{Zr}} + 3\,\mathrm{O^x_O} + \mathrm{V^{\bullet\bullet}_O}\,. \tag{1}$$

The oxygen vacancies $V_O^{\bullet\bullet}$ allow for the transport of the oxide ions. The limited oxide vacancy saturation and/or depletion near the electrolyte boundary [1] limits the concentration of the oxide ions and/or vacancies available for the charge-transfer reactions. The materials of choice for the electron-conductive phase are usually oxide perovskites [2] which often exhibit mixed ionic electronic conductivity. The present study will focus on the Lanthanum Strontium Manganite $La_{1-x}Sr_x\,MnO_3$ (LSM) which is reportedly a pure electronic conductor [3]. The DFT-calculated pathways of oxygen adsorption, dissociation, reduction and integration on the LSM surface [4] suggest that the rate-determining process is the encounter of the surface vacancy and the adsorbed oxygen ion. The surface LSM kinetics is also affected by a build-up of a potential difference between the surface and bulk [5].

The literature treating the continuum modeling of the YSZ|LSM|$O_2$ interface is mainly interested in the oxygen reduction reaction (ORR) [6–10] rather than the oxygen oxidation reaction (OOR) [11]. The

DOI 10.20347/WIAS.PREPRINT.2797 Berlin 2020

continuum physics models found in the literature can be divided into two main classes: macrohomogeneous [9–11] and phase-distinguishing [6–8]. The bulk gas transport in the macrohomogeneous models is given by either Fick's law [9, 11] or the dusty gas model [10]. The YSZ and LSM faradaic bulk currents are modeled using Ohm's law. The capacitive currents are modeled as a time derivative of the double layer capacitance which is assumed to be constantly proportional to the jump of the electrochemical potentials between the YSZ and LSM phase. Moreover, the jump acts as the driving force of the charge-transfer reactions. The kinetics of charge-transfer ORR can be described by a Butler-Volmer equation [11]. More sophisticated reaction scheme featuring the Law of Mass Action kinetics can be employed. However, both possible reaction pathways, the two phase boundary (2PB) and the three phase boundary (3PB) reaction pathways, within macrohomogeneous models [9, 10] are represented as species production densities. The surface transport of the surface species is usually not considered in macrohomogeneous models since it would only add further fitting parameters.

Phase-distinguishing models employ geometrically distinct domains for the bulk and the surface phases. For example, two parallel 1D domains representing the bulk LSM and the $O_2$|LSM surface were used in [6, 7], an 1D domain representing the LSM surface was used in [8]. The transport of gaseous species is usually neglected, the transport of the bulk and surface species is modeled with Fick's law regardless if charged or neutral [6–8]. The overpotentials driving the charge-transfer reactions depend upon the change of the electrostatic potential between the respective domains. These are either treated as a boundary condition for the 3PB pathway or assumed to be constant along the 2PB [6, 7]. Hence, the 2PB pathways are represented as species production densities connecting the two domains whereas the 3PB pathway was introduced as a boundary condition at the boundary of LSM and YSZ. Bertei et al. controlled the capacitive current at the triple phase boundary [8].

Model calibrations were carried out on either composite LSM|YSZ electrodes [9–11], on pure LSM interface electrodes [8] or both [6, 7]. The experiments used for calibration were potentiostatic IV curves [6, 7], electrochemical impedance spectroscopy (EIS) at OCV [8], or a combination of the latter and former [8, 11, 9].

Although the cited literature agrees upon the oxygen adsorption and dissociation being the rate limiting step (RLS), it does not agree upon the dominant reaction pathway of the ORR. Yang et al. [9] report that the macrohomogeneous model, calibrated by EIS and IV, renders the 2PB pathway completely dominant at higher overpotentials. They conclude that the 3PB pathway contributes more current. Whereas, Banerjee and Deutschmann found using a similar model [10] the 2PB pathway current contribution being negligible compared to 3PB pathway contribution. Moreover, Gong et al. [6, 7], using a phase-distinguishing model calibrated on IV reported a transition of the dominant pathway from the 3PB to 2PB at approximately $-0.2\,\mathrm{V}$. The findings of Gong et al.'s regarding the transition were supported by Bertei et al. using a similar, although simpler, model calibrated with EIS [8]. Bertei et al. reported that the 3PB pathway cannot transfer enough charge above a certain bias and therefore assume a transition to the 2PB pathway.

Our work aims to develop a phase-distinguishing continuum model of the YSZ|LSM interface that spatially resolves the concentration profile of oxide ion vacancies the electrostatic potential in YSZ based on our previous results [12]. The 1D domain representing YSZ at its boundary will be endowed with a kinetic mechanism describing the ORR as well as the oxygen oxidation reaction (OOR). The build-up of the double layer and the bound on the concentration inherent to the model influence the chemical potential of the oxide ions available for the reactions. This effect to our best knowledge has not yet been properly represented in the literature [6–11].

Based on numerical simulations in the time and the frequency domain and a parameter fitting approach, the model is calibrated with an experimental dataset of cyclic voltammograms and open-circuit

electrochemical impedance spectra measured for 700 °C, 750 °C, 800 °C and 850 °C and 0.2 and 0.6 ratio of $O_2$:$N_2$. While our fitting approach allows to attach arbitrary weights to EIS and CV measurements, we focus on two scenarios: EIS-preferring and EIS-CV-neutral. The EIS-preferring scenario replicates well the experimental data in the vicinity of the open circuit potential and exhibits limiting currents around $-0.2\,\mathrm{V}$ and thus identifies the three phase boundary reaction pathway. Moreover, the scenario identifies a transition of the oxygen reduction rate limiting step from the electron-transfer reaction to the oxygen adsorption reaction at 760 °C. The EIS-CV-neutral scenario reproduces well the trend of the cyclic voltammograms while overestimating the forward and backward reaction rate of the oxygen adsorption and thus suggests that a different, presumably the two phase boundary, pathway is dominant at higher biases.

# 2 Experimental

## 2.1 Materials used

The following commercially available materials were used for the in-house fabrication of a SOC in a symmetrical arrangement with ring reference electrode, see Figure 1: monocrystalline $\langle 100 \rangle$ plane $ZrO_2$ – 13 % mol-$Y_2O_3$ wafer (13YSZ, Biotain Crystal Co., Ltd.), LSM (Fuelcellmaterials) and $\alpha$-terpineol (SAFC). The monocrystalline 13YSZ wafer (25 mm diameter, 1 mm thickness) was used as an electrolyte.

## 2.2 Method of preparing three electrodes button cell

To prepare WE and CE the LSM powder was mixed with $\alpha$-terpineol. The mixture was homogenized in an ultrasonic bath for 30 min. Both electrodes (circular shape, 12 mm diameter) were prepared by deposition of the mixture by a screen printing method. The WE was cast onto the polished side of the electrolyte wafer. The reference LSM electrode was added by brush to the perimeter of the non-polished side which also contained the already deposited CE. The cell was calcined at 1150 °C for three hours after deposition of the WE and then again after the deposition of the CE and RE.

## 2.3 Cell set-up and experimental procedure

The measurement cell consisted of a zirconia housing unit for the tested SOC. Corundum capillaries were used as gas inlets / outlets. Mica plates were used for SOC sealing in the housing unit. This design allowed the setup to be divided into a WE compartment and a CE/RE compartment. The whole experimental setup was placed into a vertical tubular furnace with a built-in thermocouple. In order to make sure that the RE electrochemical potential stayed constant throughout all experiments, pure $O_2$ was fed into the CE/RE compartment. On the other hand, mixtures of different $O_2$ / $N_2$ ratios (1.0, 0.8, 0.6, 0.4, 0.2 and 0.0) were fed into the WE compartment in order to establish the dependence of electrochemical properties of the LSM electrode on the $O_2$ partial pressure. To ensure a stable composition of reactants, all gaseous mixtures were fed into their specific compartments in amounts several orders larger than required by Faraday's law.

Electrochemical measurements have been performed using a coupled potentiostat and frequency analyzer (Solartron SI 1287, Solartron SI 1260, UK). In order to evaluate electrocatalytical properties of

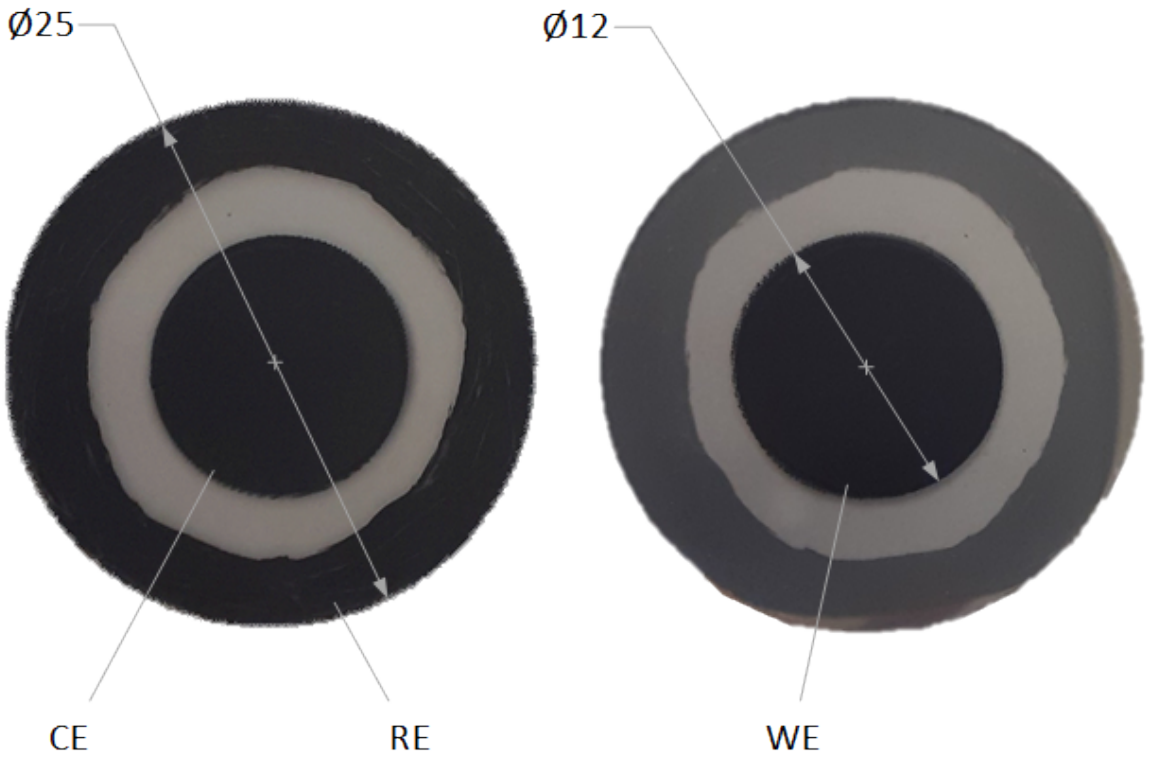


Figure 1: The counter electrode (CE) and the reference electrode (RE) are on the left. The side with the working electrode (WE) is on the right.

the LSM WE, the following electrochemical methods were used in the three electrode arrangement: Liner Sweep Cyclic Voltammetry $\langle 0; 1; -1; 0\rangle$V vs. RE with scan rate of $10\,\mathrm{mV\,s^{-1}}$, Open circuit potential (OCP) measurements to establish the stabilization of measurement conditions, and electrochemical impedance spectroscopy at OCP (frequency range from 65 kHz to 0.1 Hz with perturbing signal amplitude 50 mV).

## 3 Modeling

The model is schematically depicted in Figure 2. The bulk YSZ is represented as a one-dimensional domain carrying static positive charge and oxide ions which are modeled as an ideal lattice gas. The LSM phase and gaseous phase are represented as ideal reservoirs of electrons and oxygen. The contact of the three phases, the triple phase boundary (TPB), is represented as a point interface with surface species $O_s^{2-}$and $O^{2-}$. Two scenarios concerning the model of the surface species are introduced: ideal lattice gasses with shared and separated lattice sites. The contact of the bulk phases and TPB is provided by the adsorption reactions **A**, **E** and **O**. The electron transfer reaction $\mathbf{R}^{\Delta}$ is the only reaction of the surface species, see Equations (4).

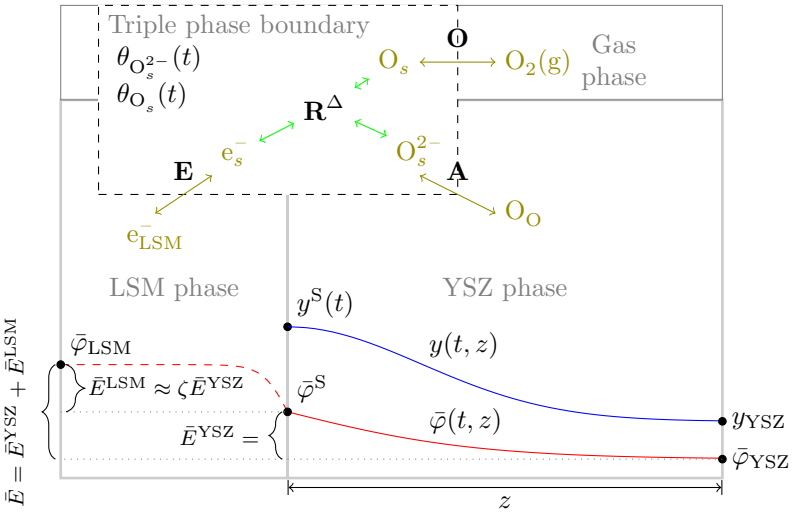


Figure 2: The species of the bulk phases $O_O^x$, $e_{LSM}^-$ and $O_2$(g) adsorb at the triple phase boundary (TPB) with the respective adsorption reactions **A**, **E** and **O**, respectively, see Equations (4). The species at TPB enter the electron transfer reaction $\mathbf{R}^\Delta$. The computational domain $\{\mathrm{TPB}\} \cup [z^S, \bar z^B]$ comprises the triple phase boundary and YSZ bulk. In the YSZ bulk $[z^S, \bar z^B]$ is simulated for the volume coverage of oxide ions $y(\bar t, \bar z)$ and the electrostatic potential $\bar\varphi(\bar t, \bar z)$. The TPB carries the surface oxide ions $O_s^{2-}$ and the surface oxygen $O_s$. The TPB is represented as a point interface $\{\mathrm{TPB}\}$ where the surface coverages $\theta_{O_s^{2-}}$ and $\theta_{O_s}$ are simulated for. The electrode potential is $\bar E := \bar\varphi^{LSM} - \bar\varphi^{YSZ}$. The potential difference controlled in the model is $\bar E^{YSZ} := \bar\varphi^S - \bar\varphi^{YSZ}$. The potential drop in LSM contributing to the electrode potential is $\bar E^{LSM} := \bar\varphi^{LSM} - \bar\varphi^S$ is approximated using the LSM charge distribution parameter $\zeta$ as $\bar E^{LSM} \approx \zeta \bar E^{YSZ}$.

## 3.1 Transport of oxides in the bulk YSZ

The bulk dimensionless model consists of the transport equation for the mobile oxide ions $O_O^x$ and the Poisson equation for the free charge density. It reads

$$\partial_{\bar t} y + \partial_{\bar z}\left[-\bar D m(1-\nu^\#)\left(\frac{\partial_{\bar z} y}{(1-y)} + \frac{z_{O_O^x}}{\bar T} y \partial_{\bar z}\bar\varphi\right)\right] = 0\,, \tag{2a}$$

$$-\lambda_d^2 \partial_{\bar z\bar z}\bar\varphi = z_{O_O^x} m(1-\nu^\#) y + z_L(x^\#, \nu^\#)\,. \tag{2b}$$

The symbols $\bar t$ and $\bar z$ denote the dimensionless time and space coordinate, respectively. The unknowns $y(\bar t, \bar z)$ and $\bar\varphi(\bar t, \bar z)$ are the volumetric coverage of the admissible anion lattice sites by the mobile oxide ions $O_O^x$ and the dimensionless electrostatic potential, respectively. Moreover, $\bar D$ and $\bar T$ are the dimensionless diffusion coefficient and temperature, respectively. The term $\lambda_d^2$ is the dimensionless dielectric permittivity. The static charge of the lattice $z_L$ depends on the $Y_2O_3$ doping $x^\#$ and the ratio of the immobile oxide ions $\nu^\#$, it reads

$$z_L(x^\#, \nu^\#) = \frac{1-x^\#}{1+x^\#} z_{Zr} + \frac{2x^\#}{1+x^\#} z_Y + m\nu^\# z_{O_O^x}\,, \tag{3}$$

where $z_{Zr} = +4, z_Y = +3, z_{O_O^x} = -2$ are the charge numbers and $m = 2$ is the ratio of the anion and cation lattice sites. $\nu^\#$ is the ratio of the immobile oxide ions to all anion lattice sites [12].

Scaling of the time, length and lattice bulk volume is chosen as

$$t = \widetilde\tau \bar t,\ z = \widetilde L \bar z,\ a_L,\ v_L\,,$$

respectively. The symbols $\widetilde{L}$ and $\widetilde{\tau}$ stand for the characteristic length and the characteristic time, respectively. The characteristic volume $v_{\mathrm{L}}$ is chosen as the volume belonging to one cation lattice site. The density of the mobile oxide ions reads

$$\rho_{=}\frac{m_{\mathrm{O}}m(1-\nu)}{v_{\mathrm{L}}}y\,,$$

where $m_{\mathrm{O}}$ denotes the atomic mass of oxygen. Energy per particle is scaled by the factor $k_{\mathrm{B}}\widetilde{T}$, therefore, the dimensionless temperature, dimensionless chemical and dimensionless electrostatic potential are defined as

$$\bar{T}=\frac{T}{\widetilde{T}},\ \bar{\mu}_{\alpha}=\frac{\mu_{\alpha}}{k_{\mathrm{B}}\widetilde{T}},\ \bar{\varphi}=\frac{e_0}{k_{\mathrm{B}}\widetilde{T}}\varphi\,,$$

respectively. Here $k_{\mathrm{B}}$ denotes the Boltzmann constant and $e_0$ is the elementary charge. The diffusion coefficient $D$ is scaled according to its physical units as

$$D=\frac{\widetilde{L}^2}{\widetilde{\tau}}\bar{D}\,.$$

Finally, the dimensionless dielectric permittivity reads

$$\lambda_{\mathrm{d}}^2=\frac{\varepsilon_0(1+\chi)k_{\mathrm{B}}\widetilde{T}}{e_0^2}\frac{v_{\mathrm{L}}}{\widetilde{L}^2}\,,$$

where $\chi$ stands for the dielectric susceptibility.

The transport of the oxide ions is assumed to be isothermal.

## 3.2 Triple phase boundary model

The TPB is assumed to carry the adsorbed oxygen atoms $\mathrm{O}_s$, the adsorbed oxide ions $\mathrm{O}_s^{2-}$, and surface electrons $\mathrm{e}^-$(s). The adsorbed species $\mathrm{O}_s$and $\mathrm{O}_s^{2-}$are modeled as surface lattice gasses. Two different types of surface lattices will be considered: shared and separated. The shared lattice model (SHA) assumes that $\mathrm{O}_s$ and $\mathrm{O}_s^{2-}$compete for the same lattice sites, therefore, their respective vacancies are equal $\mathrm{V}_{\mathrm{O}_{\mathrm{s}}^{2-}}=\mathrm{V}_{\mathrm{O}_{\mathrm{s}}}$. The separated lattice model (SEP) assumes that $\mathrm{O}_s$ and $\mathrm{O}_s^{2-}$occupy two different non-interacting lattices which leaves their respective vacancies distinguished, $\mathrm{V}_{\mathrm{O}_{\mathrm{s}}^{2-}}\neq\mathrm{V}_{\mathrm{O}_{\mathrm{s}}}$. The superscript $\Delta\in\{\mathrm{SHA},\mathrm{SEP}\}$ will be used throughout the manuscript to denote the parts of the model which depend on the lattice site model.

The contact of the three bulk phases is provided by the following adsorption reactions,

$$(\mathbf{A}):\quad \mathrm{O}_s^{2-}(\mathrm{s})+\mathrm{V}_{\mathrm{O}}^{\bullet\bullet}(\mathrm{YSZ})\rightleftharpoons\mathrm{O}_{\mathrm{O}}^{\mathrm{x}}(\mathrm{YSZ})+\mathrm{V}_{\mathrm{O}_{\mathrm{s}}^{2-}}(\mathrm{s})\,, \tag{4a}$$

$$(\mathbf{E}):\quad \mathrm{e}^-(\mathrm{LSM})\rightleftharpoons\mathrm{e}^-(\mathrm{s})\,, \tag{4b}$$

$$(\mathbf{O}):\quad \mathrm{O}_2(\mathrm{g})+2\,\mathrm{V}_{\mathrm{O}_{\mathrm{s}}}(\mathrm{s})\rightleftharpoons 2\,\mathrm{O}_s(\mathrm{s})\,. \tag{4c}$$

The symbol (s) denotes a species residing at the TPB. The TPB species are assumed to take part in the following electron-transfer reaction $\mathbf{R}^{\Delta}$,

$$(\mathbf{R}^{\mathrm{SHA}}):\quad \mathrm{O}_s(\mathrm{s})+2\,\mathrm{e}_s^-(\mathrm{s})\rightleftharpoons\mathrm{O}_s^{2-}(\mathrm{s})\,, \tag{4d}$$

$$(\mathbf{R}^{\mathrm{SEP}}):\quad \mathrm{O}_s(\mathrm{s})+2\,\mathrm{e}_s^-(\mathrm{s})+\mathrm{V}_{\mathrm{O}_{\mathrm{s}}^{2-}(\mathrm{s})}\rightleftharpoons\mathrm{O}_s^{2-}(\mathrm{s})+\mathrm{V}_{\mathrm{O}_{\mathrm{s}}}(\mathrm{s})\,. \tag{4e}$$

Note that the first electron-transfer reaction conserves the TPB vacancies whereas the additional does not.

**Chemical potentials in the bulk phases** The $O_2$(g) is modeled as an ideal gas. The chemical potential of $O_O^x$(YSZ) is modeled as an ideal lattice gas consistently with the drift-diffusion flux in equation (2). The concentration of $\mathrm{e}^-(\mathrm{LSM})$ is assumed to remain constant for all further considered processes. Therefore, the chemical potential of $e^-$(LSM) depends only on the temperature. The chemical potentials of the bulk species are, as follows,

$$\bar{\mu}_{\mathrm{O}_2} = \bar{\mu}^{ref}_{\mathrm{O}_2}(\bar{T}) + \bar{T}\log \bar{p}_{\mathrm{O}_2}\,, \tag{5a}$$

$$\bar{\mu}_{\mathrm{O}^{\mathrm{x}}_{\mathrm{O}}} = \bar{\mu}^{ref}_{\mathrm{O}^{\mathrm{x}}_{\mathrm{O}}}(\bar{T}) + \bar{T}\log\frac{y}{1-y}\,, \tag{5b}$$

$$\bar{\mu}_{\mathrm{e}^-,\mathrm{LSM}} = \bar{\mu}^{ref}_{\mathrm{e}^-,\mathrm{LSM}}(\bar{T})\,. \tag{5c}$$

Here $\bar{p}_{\mathrm{O}_2} = \frac{p_{\mathrm{O}_2}}{p^{ref}}$ is the (dimensionless) relative pressure of oxygen.

**Chemical potentials on TPB, shared and separated vacancies** The TPB coverages of the vacancies for the two scenarios read

$$\text{shared vacancies (SHA):}\quad \theta^{\mathrm{SHA}}_{\mathrm{V}_{\mathrm{O}^{2-}_s}} = \theta^{\mathrm{SHA}}_{\mathrm{V}_{\mathrm{O}_s}} = 1-\theta_{\mathrm{O}_s}-\theta_{\mathrm{O}^{2-}_s}\,, \tag{6a}$$

$$\text{separate vacancies (SEP):}\quad \theta^{\mathrm{SEP}}_{V_{\mathrm{O}^{2-}_s}} = 1-\theta_{\mathrm{O}^{2-}_s},\quad \theta^{\mathrm{SEP}}_{\mathrm{V}_{\mathrm{O}_s}} = 1-\theta_{\mathrm{O}_s}\,. \tag{6b}$$

The TPB species $O_s$ and $O_s^{2-}$ are modeled as ideal gasses on a (shared/separated) TPB lattice. The chemical potentials of TPB species read

$$\bar{\mu}^{\Delta}_{\mathrm{O}^{2-}_s}(\bar{T}) = \bar{\mu}^{ref}_{\mathrm{O}^{2-}_s} + \bar{T}\log\frac{\theta_{\mathrm{O}^{2-}_s}}{\theta^{\Delta}_{V_{\mathrm{O}^{2-}_s}}}\,, \tag{7a}$$

$$\bar{\mu}^{\Delta}_{\mathrm{O}_s}(\bar{T}) = \bar{\mu}^{ref}_{\mathrm{O}_s} + \bar{T}\log\frac{\theta_{\mathrm{O}_s}}{\theta^{\Delta}_{V_{\mathrm{O}_s}}}\,, \tag{7b}$$

where $\Delta \in \{\mathrm{SHA}, \mathrm{SEP}\}$.

### 3.2.1 Mass balances on TPB

The TPB density of species $\rho_\alpha$ is related to its surface coverage $\theta_\alpha$ as follows,

$$\rho_\alpha = m_\alpha \frac{C^{\Delta}_{\alpha}}{a_{\mathrm{L}}}\theta_\alpha,\quad \alpha \in \{\mathrm{O}^{2-}_s, \mathrm{O}_s\}\,, \tag{8}$$

where $a_{\mathrm{L}} = v_{\mathrm{L}}^{\frac{2}{3}}$ is the crystalline face area and $C_\alpha \geq 1$ relates the density of the adsorption sites for species $\alpha$ to the surface density of the crystalline lattice. The rate of the surface reaction will be scaled as

$$r^{\mathrm{X}} = \frac{1}{a_{\mathrm{L}}\widetilde{\tau}}\bar{r}^{\mathrm{X}},\quad \mathrm{X} \in \{\textbf{A, E, O, R}^{\Delta}\}\,. \tag{9}$$

The dimensionless surface mass balances reads

$$C^{\Delta}_{\mathrm{O}^{2-}}\partial_{\bar{t}}\theta_{\mathrm{O}^{2-}_s} = \bar{r}^{\mathrm{R},\Delta} - \bar{r}^{\mathrm{A}}\,, \tag{10a}$$

$$C^{\Delta}_{\mathrm{O}}\partial_{\bar{t}}\theta_{\mathrm{O}_s} = 2\bar{r}^{\mathrm{O}} - \bar{r}^{\mathrm{R},\Delta}\,, \tag{10b}$$

where $\bar{r}^{\mathrm{R}}$, $\bar{r}^{\mathrm{A}}$ and $\bar{r}^{\mathrm{O}}$ stand for the rate of the electron transfer reaction (**R**), $O^{2-}$ adsorption reaction (**A**), and the $O_2$ adsorption reaction (**O**), respectively. Note that for the SHA scenario $C^{\mathrm{SHA}}_{\mathrm{O}^{2-}} = C^{\mathrm{SHA}}_{\mathrm{O}}$, whereas for the SEP scenario are the values $C^{\mathrm{SEP}}_{\mathrm{O}^{2-}}$ and $C^{\mathrm{SEP}}_{\mathrm{O}}$ in principle independent.

### 3.2.2 General kinetics

Let us assume a general reaction of species $A_\alpha \in M = \{\mathrm{O}_s^{2-}, \mathrm{O}^{2-}, \mathrm{O}_s, \mathrm{O}_2, \mathrm{e}^-\}$,

$$\sum_{\alpha\in M} a_\alpha^i \mathrm{A}_\alpha \rightleftharpoons \sum_{\alpha\in M} b_\alpha^i \mathrm{A}_\alpha, \quad a_\alpha^i, b_\alpha^i \in \mathbb{N}_0 \,. \tag{11}$$

Clearly, the reactions (4) can be formulated in terms of (11). The stoichiometric coefficients for the $i$-th reaction are defined as $\gamma_\alpha^i := b_\alpha^i - a_\alpha^i$. The rate of reaction $r^i$ is modeled by the following product,

$$\bar{r}^i = \bar{r}_0^i(T)\, L^{i,\Delta}(\theta_\alpha, y_0, \kappa^i, S^i)\, H^i\left(\beta^i, S^i, \frac{\bar{\mathcal{A}}^i}{\bar{T}}\right) \,, \tag{12a}$$

where $\bar{\mathcal{A}}^i := \sum_{\alpha\in M} \gamma_\alpha^i \bar{\mu}_\alpha$ is the chemical affinity of the $i$-th reaction and $y_0 = y(z = \mathrm{TPB})$. The exponential part of the kinetics reads

$$H^i\left(\beta^i, S^i, \frac{\bar{\mathcal{A}}^i}{\bar{T}}\right) = \left[\exp\left(\beta^i S^i \frac{\bar{\mathcal{A}}^i}{\bar{T}}\right) - \exp\left(-(1-\beta^i) S^i \frac{\bar{\mathcal{A}}^i}{\bar{T}}\right)\right] . \tag{12b}$$

and the proportionality coefficients read

$$L^{i,\mathrm{SHA}} = \left[ y_0^{|\gamma_{\mathrm{O}^{2-}}|} (1-y_0)^{|\gamma_{\mathrm{O}^{2-}}|} \left(\theta^{\mathrm{SHA}}_{\mathrm{V}_{\mathrm{O}_s}}\right)^{\left|\gamma_{\mathrm{O}_s}+\gamma_{\mathrm{O}_s^{2-}}\right|} \theta_{\mathrm{O}_s^{2-}}^{|\gamma_{\mathrm{O}_s^{2-}}|} \theta_{\mathrm{O}_s}^{|\gamma_{\mathrm{O}_s}|} \right]^{\frac{S^i\kappa^i}{2}} , \tag{12c}$$

$$L^{i,\mathrm{SEP}} = \left[ y_0^{|\gamma_{\mathrm{O}^{2-}}|} (1-y_0)^{|\gamma_{\mathrm{O}^{2-}}|} \left(\theta^{\mathrm{SEP}}_{\mathrm{V}_{\mathrm{O}_s}}\right)^{|\gamma_{\mathrm{O}_s}|} \left(\theta^{\mathrm{SEP}}_{\mathrm{V}_{\mathrm{O}_s^{2-}}}\right)^{|\gamma_{\mathrm{O}_s^{2-}}|} \theta_{\mathrm{O}_s^{2-}}^{|\gamma_{\mathrm{O}_s^{2-}}|} \theta_{\mathrm{O}_s}^{|\gamma_{\mathrm{O}_s}|} \right]^{\frac{S^i\kappa^i}{2}} . \tag{12d}$$

The parameters have the following properties

$$\beta^i, \kappa^i \in [0,1],\ S^i > 0, \quad \text{and} \quad \bar{r}_0^i(T) \geq 0 \,. \tag{12e}$$

The parameter $S^i$ can be adjusted to account for the freedom in the scaling of the stoichiometry of the reaction. The $\bar{r}_0^i(T)$ is the (dimensionless) frequency rate. The kinetics given by formula (12a) respects the thermodynamic equilibrium and direction of the reaction due the virtue of (12b).

We will limit our choice of the $\kappa^i$ and $\beta^i$ with the two kinetic scenarios in the remainder of the manuscript, that is,

$$\text{EXP kinetics: } \kappa^i = 0 \,, \tag{12f}$$

$$\text{LoMA kinetics: } \kappa^i = 1,\ \beta^i = \frac{1}{2} \,. \tag{12g}$$

### 3.2.3 Kinetics of adsorption reactions

**Electron adsorption (E)** The transport of electrons in the LSM is assumed to be fast compared to the rest of the described processes, therefore, we assume that the electrons are at all instances in a convection-diffusion equilibrium. This assumption also implies that the electron adsorption reaction (4b) is in equilibrium. Therefore, we set the electrochemical potential of electrons in LSM, see (5c), equal to the electrochemical potential of the electrons at TPB, i.e.,

$$\bar{\mu}_{\mathrm{e}^-}\Big|_{\bar{z}=\mathrm{TPB}} + z_{\mathrm{e}^-}\bar{\varphi}^{\mathrm{S}} = \bar{\mu}^{ref}_{\mathrm{e}^-,\mathrm{LSM}}(\bar{T}) + z_{\mathrm{e}^-}\bar{\varphi}\Big|_{\bar{z}=\mathrm{LSM}} \,, \tag{13}$$

where the abbreviation $\bar{\varphi}_0 = \bar{\varphi}(\bar{z} = \mathrm{TPB})$ is employed.

**Adsorption of bulk $O^{2-}$ ions (A)** The affinity of the adsorption reaction (4a) reads

$$\bar{\mathcal{A}}^{\mathrm{A}} = -\Delta\bar{G}^{\mathrm{A}} + \bar{T}\log\left[\frac{\theta_{\mathrm{O}_s^{2-}}}{\theta^{\Delta}_{\mathrm{V}_{\mathrm{O}_s^{2-}}}}\frac{1-y_0}{y_0}\right], \tag{14}$$

where the change of the Gibbs free energy is defined as $\Delta\bar{G}^{\mathrm{A}} := \bar{\mu}^{\mathrm{ref}}_{\mathrm{O}^{2-}} - \bar{\mu}^{\mathrm{ref}}_{\mathrm{O}_s^{2-}}$. The rate of the oxide adsorption $\mathbf{A}$ reads

$$\begin{aligned}\bar{r}^{\mathrm{A}} = \bar{r}_0^{\mathrm{A}}\left[y_0(1-y_0)\theta_{\mathrm{O}_s^{2-}}\theta^{\Delta}_{\mathrm{V}_{\mathrm{O}_s^{2-}}}\right]^{\frac{S^{\mathrm{A}}\kappa^{\mathrm{A}}}{2}}\Bigg[e^{-\frac{\beta^{\mathrm{A}}S^{\mathrm{A}}}{\bar{T}}\left(\Delta\bar{G}^{\mathrm{A}}\right)}\left(\frac{y_0}{1-y_0}\frac{\theta^{\Delta}_{\mathrm{V}_{\mathrm{O}_s^{2-}}}}{\theta_{\mathrm{O}_s^{2-}}}\right)^{-\beta^{\mathrm{A}}S^{\mathrm{A}}} \\ - e^{\frac{(1-\beta^{\mathrm{A}})S^{\mathrm{A}}}{\bar{T}}\left(\Delta\bar{G}^{\mathrm{A}}\right)}\left(\frac{y_0}{1-y_0}\frac{\theta^{\Delta}_{\mathrm{V}_{\mathrm{O}_s^{2-}}}}{\theta_{\mathrm{O}_s^{2-}}}\right)^{(1-\beta^{\mathrm{A}})S^{\mathrm{A}}}\Bigg].\end{aligned} \tag{15}$$

**Adsorption of oxygen (O)** The affinity of the dissociative oxygen adsorption (4c) reads

$$\bar{\mathcal{A}}^{\mathrm{O}} = -\Delta\bar{G}^{\mathrm{O}} + \bar{T}\log\left[\left(\frac{\theta^{\Delta}_{\mathrm{V}_{\mathrm{O}_s}}}{\theta_{\mathrm{O}_s}}\right)^2\bar{p}_{\mathrm{O}_2}\right], \tag{16}$$

where $\Delta\bar{G}^{\mathrm{O}} := 2\bar{\mu}^{\mathrm{ref}}_{\mathrm{O}_s} - \bar{\mu}^{\mathrm{ref}}_{\mathrm{O}_2}$. The rate of the oxygen adsorption **O** reads

$$\begin{aligned}\bar{r}^{\mathrm{O}} = \bar{r}_0^{\mathrm{O}}\left[\theta^2_{\mathrm{O}_s}\left(\theta^{\Delta}_{\mathrm{V}_{\mathrm{O}_s}}\right)^2\bar{p}_{\mathrm{O}_2}\right]^{\frac{S^{\mathrm{O}}\kappa^{\mathrm{O}}}{2}}\Bigg[e^{-\beta^{\mathrm{O}}S^{\mathrm{O}}\frac{\Delta\bar{G}^{\mathrm{O}}}{\bar{T}}}\left(\left(\frac{\theta_{\mathrm{O}_s}}{\theta^{\Delta}_{\mathrm{V}_{\mathrm{O}_s}}}\right)^2\frac{1}{\bar{p}_{\mathrm{O}_2}}\right)^{-\beta^{\mathrm{O}}S^{\mathrm{O}}} \\ - e^{(1-\beta^{\mathrm{O}})S^{\mathrm{O}}\frac{\delta\bar{G}^{\mathrm{O}}}{\bar{T}}}\left(\left(\frac{\theta_{\mathrm{O}_s}}{\theta^{\Delta}_{\mathrm{V}_{\mathrm{O}_s}}}\right)^2\frac{1}{\bar{p}_{\mathrm{O}_2}}\right)^{(1-\beta^{\mathrm{O}})S^{\mathrm{O}}}\Bigg].\end{aligned} \tag{17}$$

### 3.2.4 Electron transfer reaction kinetics

Modeling of the chemical potential of the electrons at TPB is beyond the scope of this work. Therefore, the drift-diffusion-reaction equilibrium condition (13) will be introduced in to the affinity of the electron reaction and thereby the cumbersome term $\bar{\mu}_{\mathrm{e}^-,s}$ will be replaced by $\bar{\mu}_{\mathrm{e}^-,\mathrm{LSM}}(\bar{T})$ and the potential difference $\bar{E}^{\mathrm{LSM}}$. The calculation proceeds as follows

$$\begin{aligned}\bar{\mathcal{R}}^{\mathrm{E}} &= \bar{\mu}^{\Delta}_{\mathrm{O}_s} + \left(2\bar{\mu}_{\mathrm{e}^-} - \bar{\mu}^{\Delta}_{\mathrm{O}_s^{2-}}\right) + \underbrace{\left(2z_{\mathrm{e}^-} - z_{\mathrm{O}^{\mathrm{x}}}\right)}_{=0}\bar{\varphi}^{\mathrm{S}} \\ &\overset{(13)}{=} \bar{\mu}_{\mathrm{O}_s} + 2\left(\bar{\mu}^{\mathrm{ref}}_{\mathrm{e}^-,\mathrm{LSM}} + z_{\mathrm{e}^-}\bar{\varphi}^{\mathrm{LSM}}\right) - \left(\bar{\mu}_{\mathrm{O}_s^{2-}} + z_{\mathrm{O}_s^{2-}}\bar{\varphi}^{\mathrm{S}}\right) \\ &= \bar{\mu}_{\mathrm{O}_s} + 2\bar{\mu}^{\mathrm{ref}}_{\mathrm{e}^-,\mathrm{LSM}} - \bar{\mu}_{\mathrm{O}_s^{2-}} + \underbrace{2z_{\mathrm{e}^-}\bar{\varphi}^{\mathrm{LSM}} - z_{\mathrm{O}_s^{2-}}\bar{\varphi}^{\mathrm{S}}}_{=:-2\bar{E}^{\mathrm{LSM}}} \\ &\approx -\Delta\bar{G}^{\mathrm{R}} + \bar{T}\log\left[\frac{\theta_{\mathrm{O}}}{\theta^{\Delta}_{V_{\mathrm{O}}}}\frac{\theta^{\Delta}_{\mathrm{V}_{\mathrm{O}_s^{2-}}}}{\theta_{\mathrm{O}_s^{2-}}}\right] - 2\zeta\bar{E}^{\mathrm{YSZ}},\end{aligned}$$

where $\Delta\bar{G}^{\mathrm{R}} := -\bar{\mu}^{\mathrm{ref}}_{\mathrm{O}_s} - 2\bar{\mu}^{\mathrm{ref}}_{\mathrm{e}^-,\mathrm{LSM}} + \bar{\mu}^{\mathrm{ref}}_{\mathrm{O}^{2-}_s}$ and $\bar{\varphi}^{\mathrm{LSM}} := \bar{\varphi}|_{\bar{z}=\mathsf{LSM}}$. The contribution to the electrode potential from the LSM phase $\bar{E}^{\mathrm{LSM}}$ and the electrode potential contribution from the YSZ phase $\bar{E}^{\mathrm{YSZ}}$ are defined as

$$\bar{E}^{\mathrm{LSM}} := \bar{\varphi}^{\mathrm{LSM}} - \bar{\varphi}^{\mathrm{S}} \,, \tag{18}$$

$$\bar{E}^{\mathrm{YSZ}} := (\bar{\varphi}^{\mathrm{S}} - \bar{\varphi}|_{\bar{z}=\mathrm{YSZ}}) \,, \tag{19}$$

respectively. The precise definition of $\bar{\varphi}^{\mathrm{YSZ}}$ is given in equation (27). Since $E^{\mathrm{LSM}}$ is not controlled in the model, see Figure 2, we choose to approximate its value as follows,

$$\bar{E}^{\mathrm{LSM}} \approx \zeta \bar{E}^{\mathrm{YSZ}} \,, \tag{20}$$

where $\zeta$ is the LSM charge distribution parameter. The scaling factor $L^{\mathrm{R},\Delta}$ reads, for the case of the separate lattice sites as

$$L^{\mathrm{R,\,SEP}} = \frac{1}{S^{\mathrm{R}}} \left[ \theta_{\mathrm{O}_s} \theta^{\mathrm{SEP}}_{\mathrm{V}_{\mathrm{O}_s}} \theta_{\mathrm{O}^{2-}_s} \theta^{\mathrm{SEP}}_{\mathrm{V}_{\mathrm{O}^{2-}_s}} \right]^{\frac{S^{\mathrm{R}}{}_{\kappa^{\mathrm{R}}}}{2}} \,. \tag{21}$$

In the case of shared lattice sites, it reads

$$L^{\mathrm{R,\,SHA}} = \frac{1}{S^{\mathrm{R}}} \left[ \theta_{\mathrm{O}_s} \theta_{\mathrm{O}^{2-}_s} \right]^{\frac{S^{\mathrm{R}}{}_{\kappa^{\mathrm{R}}}}{2}} \,. \tag{22}$$

Note that the $L^{\mathrm{R,SHA}}$ does not translate into $L^{\mathrm{R,SEP}}$ when the formula (6a) is employed. Finally, the reaction rate of the electron-transfer reactions read

$$\begin{aligned} \bar{r}^{\mathrm{R},\Delta} = \bar{r}^{\mathrm{R}}_0 L^{\mathrm{R},\Delta} \Bigg[ & e^{-\frac{\beta^{\mathrm{R}} S^{\mathrm{R}}}{T}\left(\Delta G^{\mathrm{R}} + 2\zeta \bar{E}^{\mathrm{YSZ}}\right)} \left( \frac{\theta^{\Delta}_{V_{\mathrm{O}}}}{\theta_{\mathrm{O}}} \frac{\theta_{\mathrm{O}^{2-}_s}}{\theta^{\Delta}_{V_{\mathrm{O}^{2-}_s}}} \right)^{-\beta^{\mathrm{R}} S^{\mathrm{R}}} \\ & - e^{\frac{(1-\beta^{\mathrm{R}}) S^{\mathrm{R}}}{T}\left(\Delta G^{\mathrm{R}} + 2\zeta \bar{E}^{\mathrm{YSZ}}\right)} \left( \frac{\theta^{\Delta}_{V_{\mathrm{O}}}}{\theta_{\mathrm{O}}} \frac{\theta_{\mathrm{O}^{2-}_s}}{\theta^{\Delta}_{V_{\mathrm{O}^{2-}_s}}} \right)^{(1-\beta^{\mathrm{R}}) S^{\mathrm{R}}} \Bigg] \,, \end{aligned} \tag{23}$$

for $\Delta \in \{\mathrm{SHA}, \mathrm{SEP}\}$, see (6a). Note that for the shared sites scenario do the vacancy coverages cancel out in (23).

## 3.3 Equilibrium

For a given electroneutral coverage of oxide ions in YSZ $y(\bar{z} = \mathrm{bulk\,YSZ}) = y_{\mathsf{B}}$ and partial pressure of oxygen $\bar{p}_{\mathrm{O}_2}$, the equilibrium state $y^{\mathrm{eq}}, \bar{E}^{\mathrm{YSZ}}_{\mathrm{eq}}, \theta^{\mathrm{eq}}_{\mathrm{O}^{2-}_s}, \theta^{\mathrm{eq}}_{\mathrm{O}_s}$ is defined as a solution of the governing equations (2) and (10) for which the bulk flux of the oxide ions (2) and the rates of the chemical reactions (16), (18) and (23) vanish. These assertions result in the following, telescopic, system of

equations,

$$\frac{y^{\mathrm{B}}}{1-y^{\mathrm{B}}} = \frac{y_0^{\mathrm{eq}}}{1-y_0^{\mathrm{eq}}} \exp\left(\frac{z_{\mathrm{A}}\bar{E}_{\mathrm{eq}}^{\mathrm{YSZ}}}{\bar{T}}\right) , \tag{24a}$$

$$\frac{y_0^{\mathrm{eq}}}{1-y_0^{\mathrm{eq}}} = \frac{\theta_{\mathrm{O}_s^{2-}}^{\mathrm{eq}}}{\theta_{\mathrm{V}_{\mathrm{O}_s^{2-}}}^{\Delta,\mathrm{eq}}} \exp\left(\frac{\Delta\bar{G}^{\mathrm{A}}}{\bar{T}}\right) , \tag{24b}$$

$$\frac{\theta_{\mathrm{O}_s^{2-}}^{\mathrm{eq}}}{\theta_{\mathrm{V}_{\mathrm{O}_s^{2-}}}^{\Delta,\mathrm{eq}}} = \frac{\theta_{\mathrm{O}_s}^{\mathrm{eq}}}{\theta_{\mathrm{V}_{\mathrm{O}_s}}^{\Delta,\mathrm{eq}}} \exp\left(\frac{\Delta\bar{G}^{\mathrm{R}} + \zeta 2\bar{E}_{\mathrm{eq}}^{\mathrm{YSZ}}}{\bar{T}}\right) , \tag{24c}$$

$$\frac{\theta_{\mathrm{O}_s}^{\mathrm{eq}}}{\theta_{\mathrm{V}_{\mathrm{O}_s}}^{\Delta,\mathrm{eq}}} = \sqrt{\bar{p}_{\mathrm{O}_2}^{\mathrm{eq}}} \exp\left(\frac{\Delta\bar{G}^{\mathrm{O}}}{2\bar{T}}\right) . \tag{24d}$$

The YSZ part of electrode potential difference in equilibrium reads

$$\bar{E}_{\mathrm{eq}}^{\mathrm{YSZ}} = \frac{\bar{T}\left(\ln\frac{y_0^{\mathrm{eq}}}{1-y_0^{\mathrm{eq}}} - \ln\sqrt{\bar{p}_{\mathrm{O}_2}}\right) - \frac{\Delta\bar{G}^{\mathrm{O}}}{2} - \Delta\bar{G}^{\mathrm{R}} - \Delta\bar{G}^{\mathrm{A}}}{2(\zeta+1)} . \tag{25}$$

## 3.4 Boundary conditions

### 3.4.1 Dirichlet boundary condition for electrostatic potential

The Dirichlet boundary condition in the YSZ bulk is $\bar{\varphi}^{\mathrm{B}} = 0$. Instead of imposing directly the Dirichlet boundary condition $\bar{\varphi}^{\mathrm{S}}$ at the TPB, the electrostatic potential in the working electrode $\bar{\varphi}^{\mathrm{LSM}}$ is chosen to be the driving parameter. The electric potential at the TPB $\bar{\varphi}^{\mathrm{S}}$ is implicitly calculated within the simulation as

$$\bar{\varphi}^{\mathrm{S}} = \bar{\varphi}^{\mathrm{LSM}} - \bar{E}^{\mathrm{LSM}} \overset{(20)}{=} \bar{\varphi}^{\mathrm{LSM}} - \zeta\bar{E}^{\mathrm{YSZ}} = \bar{\varphi}^{\mathrm{LSM}} - \zeta(\bar{\varphi}^{\mathrm{S}} - \bar{\varphi}^{\mathrm{YSZ}}) . \tag{26}$$

The value $\bar{\varphi}^{\mathrm{YSZ}}$ is approximated, as follows,

$$\bar{\varphi}^{\mathrm{YSZ}} \approx \bar{\varphi}^{\mathrm{B}} + \frac{\bar{\varphi}^{\mathrm{B}} - \bar{\varphi}(X)}{\bar{L} - \bar{X}}(0 - \bar{L}) , \tag{27}$$

for $\bar{X} \in (0+\epsilon, \bar{L})$ since the IR slope in the bulk YSZ is linear. $\bar{L}$ is the length of the simulation domain. The $\epsilon \ll 1$ is chosen as a multiple of the double layer length. The simulation voltage $U^{\mathrm{sim}}$ and the simulation overvoltage $\eta^{\mathrm{sim}}$ are defined as

$$\bar{U}^{\mathrm{sim}} = \bar{\varphi}^{\mathrm{LSM}} - \bar{\varphi}^{\mathrm{B}} , \tag{28}$$

$$\bar{\eta}^{\mathrm{sim}} = \bar{U}^{\mathrm{sim}} - \bar{U}_{\mathrm{eq}}^{\mathrm{sim}} , \tag{29}$$

where $\bar{U}_{\mathrm{eq}}^{\mathrm{sim}} = \bar{E}_{\mathrm{eq}}^{\mathrm{LSM}} + \bar{E}_{\mathrm{eq}}^{\mathrm{YSZ}}$ is the equilibrium value of the simulation voltage. The choice of the driving parameter is convenient in order to match the experimental measurements, see Section 3.4.4 and Figure 3.

### 3.4.2 Boundary reaction condition

The normal bulk flux of the oxide ions at the TPB is equal to its production due to the adsorption reaction, as follows,

$$-\bar{D}m(1-\nu^{\#})\left(\frac{\partial_{\bar{z}}y}{(1-y)}+\frac{z_{\mathrm{O}_{\mathrm{O}}^{\mathrm{x}}}C_{\mathrm{O}_s^{2-}}y}{\bar{T}}\partial_{\bar{z}}\bar{\varphi}\right)\nu\Big|_{\bar{z}^{\mathrm{S}}}=\frac{v_{\mathrm{L}}}{\widetilde{L}a_{\mathrm{L}}m(1-\nu^{\#})}\bar{r}^{\mathrm{A}}\,.$$

### 3.4.3 Electric current

Current density of electrons in LSM electrode reads

$$\begin{aligned}j_{\mathrm{e}^-}|_{\mathsf{LSM}}=&-\frac{e_0\widetilde{L}}{v_{\mathrm{L}}\widetilde{\tau}}\frac{\mathrm{d}}{\mathrm{d}\bar{t}}\int_{\bar{z}^{\mathrm{S}}}^{\bar{z}^{\mathrm{B}}}\left(z_{\mathrm{O}_{\mathrm{O}}^{\mathrm{x}}}m(1-\nu^{\#})y(\bar{z})+z_{\mathrm{L}}\right)\mathrm{d}\bar{z}\\&-\frac{e_0z_{\mathrm{O}_s^{2-}}C_{\mathrm{O}_s^{2-}}}{a_{\mathrm{L}}\widetilde{\tau}}\frac{\mathrm{d}}{\mathrm{d}\bar{t}}\theta_{\mathrm{O}_s^{2-}}\\&-\varepsilon_0(1+\chi)\frac{k_{\mathrm{B}}\widetilde{T}}{e_0\widetilde{L}\widetilde{\tau}}\frac{\mathrm{d}}{\mathrm{d}\bar{t}}\frac{\mathrm{d}}{\mathrm{d}\bar{z}}\bar{\varphi}^{\mathrm{B}}\nu\\&+\frac{\gamma_{\mathrm{e}^-}^{\mathbf{R}}e_0z_{\mathrm{e}^-}}{a_{\mathrm{L}}\widetilde{\tau}}\bar{r}^{\mathbf{R},\Delta}.\end{aligned}\tag{30}$$

The relation of the electron current density and the electric current measured in the experiments $I$ is given as follows,

$$I=S\,j_{\mathrm{e}^-}|_{\mathsf{LSM}},\tag{31}$$

where $S$ is an active cross-section of electrode.

### 3.4.4 Overvoltage

The experimental cell consists of YSZ electrolyte and three LSM electrodes as shown in Figure 1. Assuming the same oxygen partial pressure and temperature across the cell, the schematic shape of the electrostatic potential $\bar{\varphi}$ in equilibrium and with applied positive bias are shown in the top and bottom of Figure 3, respectively. Since the ohmic loss in the LSM is assumed negligible compared to YSZ, the voltage measured in experiment reads

$$U^{\mathrm{exp}}=\varphi^{\mathrm{LSM}}-\varphi^{\mathrm{ref}}=E^{\mathrm{RE}}+IR+E\,,\tag{32}$$

where $E$ stands for the working electrode potential, $IR$ is the ohmic loss in YSZ and $E^{\mathrm{RE}}$ is the constant potential of the reference electrode. The experimental overvoltage is defined as

$$\eta^{\mathrm{exp}}=U^{\mathrm{exp}}-U_{\mathrm{eq}}^{\mathrm{exp}}=IR+(E-E_{\mathrm{eq}})\,,\tag{33}$$

where the subscript $\cdot_{\mathrm{eq}}$ denotes the quantity in equilibrium, i.e. the open-circuit conditions. The simulation overvoltage $\eta^{\mathrm{sim}}$, defined in Equation (29), is equivalent to the experimental overvoltage $\eta^{\mathrm{exp}}$,

$$\eta^{\mathrm{exp}}=IR+(E-E_{\mathrm{eq}})=\varphi^{\mathrm{B}}-\varphi^{\mathrm{LSM}}-E_{\mathrm{eq}}\overset{(29)}{=}\eta^{\mathrm{sim}}\,.\tag{34}$$

We note that IR correction of experimental data is not performed since it is implicitly included within the simulation.

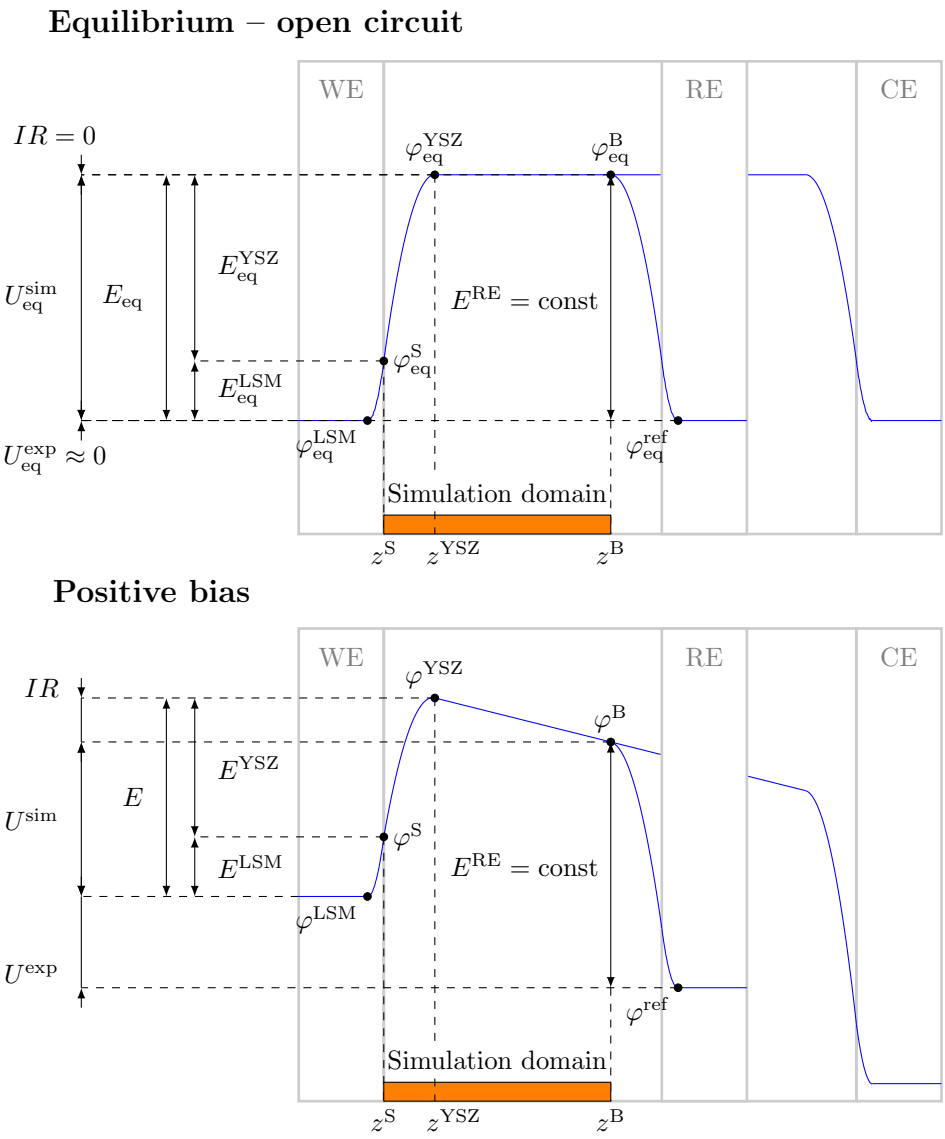


Figure 3: A schematic of the electrostatic potential shape and its relation to the working electrode potential $E$, reference electrode potential $E^{\rm RE}$ and the modeled quantities in equilibrium (top) and under applied positive bias (bottom). The simulation domain spans between TPB $z^{\rm S}$ and middle-electrolyte bulk $z^{\rm B}$. However, simulated voltage $U^{\rm sim}$ includes also $E^{\rm LSM}$ potential difference due to the approximation 20. The half-double-layer length $|z^{\rm S} - z^{\rm YSZ}|$ is typically in units of $\rm nm$, whereas the distance to reference electrode $|z^{\rm S} - z^{\rm B}| = 0.5\ \rm mm$.

## 3.5 Numerical tools

A thermodynamically consistent, exponentially fitted upwind finite volume discretization approach was used to perform the space discretization [12]. To achieve unconditional stability, the implicit Euler method was chosen for the time discretization. The numerical scheme was implemented in the Julia programming language on top of the VoronoiFVM.jl package [13]. In particular, this approach allows to handle linearization of the complex nonlinearities occurring in the model via automatic differentiation. This significantly eases the implementation of Newton's method for solving the time stepping problems, and in addition, linearization around steady state solutions, as necessary for impedance calculation.

The numerical solution for PDE was embedded into in-house made code capable of effective simulation of several experimental methods using large amount of computational resources in order to fit unknown physical parameters. The most important pieces of information will be mentioned in this section. The code is available upon request.

### 3.5.1 Implemented experimental methods

**Electrochemical impedance spectroscopy (EIS)** The system of equations and the the current formula (30) are linearized around an equilibrium state, allowing to calculate the response to a time periodic applied voltage $U^{\mathrm{sim}}$ with small amplitude by the solution of a linear system with complex unknowns in the frequency domain. The resulting very fast approach to calculate the impedance $Z$ has been successfully verified by comparison with a standard time domain simulation. We note that this approach avoids the use of equivalent models, and calculated results can be directly related to the parameters described in the model.

**Linear-sweep cyclic voltammetry (CV)** This is based on the solution of the transient problem with a saw-tooth like profile for $\varphi^{\mathrm{LSM}}$ with values between $-1\,\mathrm{V}$ and $1\,\mathrm{V}$.

### 3.5.2 Estimation of diffusion coefficient

There are two parameters to be fitted in the bulk: the diffusion coefficient $D$ and the immobile oxide ratio $\nu^{\#}$. They both influence a value of the total ohmic resistance $R^{\mathsf{Ohm}}$ which can be observed in the EIS spectrum as the high frequency limit of the real part of impedance. The value coincides with the value of resistance $R^{\mathsf{bulk}}$ of electrolyte which can be directly calculated as

$$R^{\mathsf{Ohm}} = R^{\mathsf{bulk}}(D,\nu^{\#}) := \frac{L}{S}\frac{1}{\sigma(D,\nu^{\#})}, \tag{35}$$

$$\sigma(D,\nu^{\#}) = \frac{2\mathsf{e}_0}{m_{\mathrm{O}}} D \frac{m(1-\nu^{\#})}{v_{\mathrm{L}}} y_{\mathsf{B}} \tag{36}$$

where $S$, $L$ and $\sigma$ are active cross-section area, length and conductivity of electrolyte, respectively. Other model parameters have no impact on ohmic resistance. Since ohmic resistance is an experimentally accessible quantity, it is convenient to use relation (36) to obtain $D$ as a function of $\sigma$ and $\nu^{\#}$. As conductivity $\sigma$ can be determined a priori via $R^{\mathsf{Ohm}}$, $\nu$ remains the only bulk parameter to be fitted. During the fitting algorithm, specific values of $\nu^{\#}$ then determine the value of $D(\sigma,\nu^{\#})$.

Unlike the model, measured EIS data often do not show a clear high frequency limit since inductance behavior comes into play and also high frequencies are difficult to measure with sufficient precision. There are several options to extract the necessary information. After filtering out the inductance, there is a possibility to use equivalent electric circuit or DRT analysis to extrapolate the experimental frequency range to obtain the high frequency limit.

Ohmic resistance varies with temperature but can vary also with oxygen partial pressure. Experimental data presented in section 2 show relatively similar values of the high frequency limit for each temperature. A common average ohmic resistance for each temperature was estimated with use of generalized DRT method [14]. This method allows to describe EIS data with equivalent electrical circuit consisting of RC elements in series together with ohmic resistance and inductance. Table 1 shows obtained values for ohmic resistances $R^{\mathsf{Ohm}}$ and the adjacent conductivities $\sigma$. Conductivity $\sigma$ could

be also a parameter to be fitted during the fitting procedure, but the aim is to keep the number of unknown parameters as low as possible and specifically this experimental data set allows to compute conductivities in advance.

Inductance was estimated to $2.45 \times 10^{-6}$H. This value is used for all simulations.

Table 1: Table of ohmic resistances and conductivities with respect to temperature change.

| | $700°$C | $750°$C | $800°$C | $850°$C |
|---|---|---|---|---|
| $R^{\text{Ohm}}[\Omega]$ | 6.222 | 3.066 | 1.740 | 1.065 |
| $\sigma$[S/m] | 1.015 | 2.06 | 3.63 | 5.93 |

### 3.5.3 Choice of fitness function

In order to find a suitable set of physical parameters for the model, a measure of proximity–fitness function–is defined between the experimental data and the results of numerical simulation. Our fitness function is chosen as a compromise between relative and absolute errors. Considering only the relative errors would lead into non-physical high sensitivity to small deviations of small values, which is not the desired behavior since the measurement provides imperfect data shifted by a noise with similar amplitude regardless of the magnitude of measured data. Using absolute error seems more feasible although a problem arises when comparing multiple sets of experimental data of a different magnitude. For example, lets assume a fitting process of two voltammetry data sets CV1 and CV2 with maximum current around $0.1$A and $1$A, respectively. A small (absolute) deviation from larger CV2 would lead to a larger fitness error then a–relatively–large error due to a smaller current magnitude of CV1. Hence the information hidden in the CV1 experiment would not be revealed as much as possible.

The fitness function is therefore designed so that the experimental data are multiplied by a fixed factor in order to be close to some abstract reference state. In the case of cyclic voltammetry, the maximum of the current is normed to value $1$A. The simulated data are multiplied by the same factor. The CV-fitness function is defined as a sum of the squared absolute errors of the scaled data. An analogous procedure is applied to the EIS data.

Having proper fitness functions for both EIS and CV, there is still a freedom of balancing the importance of these two types of experiment against each other while finding the optimal model parameters. We call it EIS:CV weights.

### 3.5.4 Fitting process

The numerical fitting of parameters to experiment is done using Nelder-Mead method also called downhill simplex method. A Julia language package *LeastSquaresOptim.jl* [15] is used for this purpose. In almost all practical cases, it is necessary to start from sufficiently diverse initial points of parametric space in order to rise the chance of revealing the global minimum. Firstly, the user specifies the range of initial values for each parameter (i.e having two parameters $A$ and $B$ with specified ranges $A \in \{1, 2, 3\}$ and $B \in \{10, 11, 12\}$). Secondly, the fitting routine is run on computational cluster for all combinations of initial values (i.e $(1, 10), (1, 11), (1, 12), (2, 10), \dots$). Each combination makes its own way throughout the parametric space. Typically, hundreds or thousands of individual paths are used to find the global minimum of the fitness function. For the sake of saving computational resources, it is important to test wider range only for parameters which are suspected from making

local minima (i.e. highly non-linear). In the case of the presented model, standard difference of Gibbs energy $\Delta G^{\mathrm{X}}$ is the most dangerous parameter.

# 4 Parameter space pruning based on qualitative comparison to the experiments

Table 2: Overview of fitted parameters. Symmetry factors are set to $\beta^{\mathrm{X}} = 0.5$.

| symbol | unit | ls-SHA | ls-SEP | k-EXP | k-LoMA | k-LoMA-z |
|---|---|---|---|---|---|---|
| kinetics | - | LoMA | LoMA | EXP | LoMA | LoMA |
| SHA/SEP | - | SHA | SEP | SEP | SEP | SEP |
| $\zeta$ | 1 | 0.0 | 0.0 | 0.17 | 0.0 | 0.8 |
| $\log_{10} \bar{r}_0^{\mathrm{A}}$ | $\mathrm{m}^{-2}\mathrm{s}^{-1}$ | 22.99 | 22.23 | 22.32 | 22.56 | 22.61 |
| $\log_{10} \bar{r}_0^{\mathrm{R}}$ | $\mathrm{m}^{-2}\mathrm{s}^{-1}$ | 21.96 | 22.01 | 20.65 | 22.80 | 21.79 |
| $\log_{10} \bar{r}_0^{\mathrm{O}}$ | $\mathrm{m}^{-2}\mathrm{s}^{-1}$ | 22.67 | 21.95 | 20.98 | 21.98 | 24.97 |
| $\Delta G^{\mathrm{A}}$ | eV | 0.093 | −0.114 | 0.161 | −0.043 | 0.005 |
| $\Delta G^{\mathrm{R}}$ | eV | 0.075 | 0.089 | −0.126 | 0.114 | 0.25 |
| $\Delta G^{\mathrm{O}}$ | eV | −0.615 | −0.220 | 0.071 | 0.014 | −0.013 |
| $S^{\mathrm{A}}$ | 1 | 1 | 1 | 0.383 | 0.308 | 0.410 |
| $S^{\mathrm{R}}$ | 1 | 1 | 1 | 3.8 | 2.307 | 2.123 |
| $S^{\mathrm{O}}$ | 1 | 1 | 1 | 1 | 1.045 | 1.038 |
| $\nu^{\#}$ | 1 | 0.34 | 0.324 | 0.42 | 0.3 | 0.687 |
| $C_{\mathrm{O}^{2-}}$ | 1 | 12.26 | 1.7 | 1.20 | 3.597 | 1.38 |
| $C_{\mathrm{O}}$ | 1 | 12.26 | 21.98 | 14.05 | 12.66 | 20.18 |

## 4.1 Shared versus separate lattice sites

Since the electron adsorption reaction (4b) was equilibrated (13), there are three remaining reaction reactions in the model, namely $\mathbf{A}$, $\mathbf{R}$ and $\mathbf{O}$. The imaginary part of the simulated impedance spectra reveals three distinct processes. A small perturbation in the exchange current density of one of the remaining reactions results into a shift of a single peak in the imaginary Bode diagram and thus it establishes a heuristic peak-to-reaction relation. Numerical tests show that the frequency order of the peak-to-reaction relation is stable for a broad range of parameters. The frequency ordered peak-to-reaction relations for the two scenarios are listed in Table 3.

Table 3: The peak-to-reaction relation helps to reveal the main qualitative difference between the SHA and SEP scenarios (6a).

| scenario/frequency range | low | mid | high |
|---|---|---|---|
| SHA | $\mathbf{R}$ | $\mathbf{O}$ | $\mathbf{A}$ |
| SEP | $\mathbf{O}$ | $\mathbf{R}$ | $\mathbf{A}$ |

Let us illustrate this on an experimental EIS data. Figure 4 depicts fits of a measured spectrum for the two lattice sites scenarios. The model parameters for the SEP and SHA scenarios are listed in Table 2

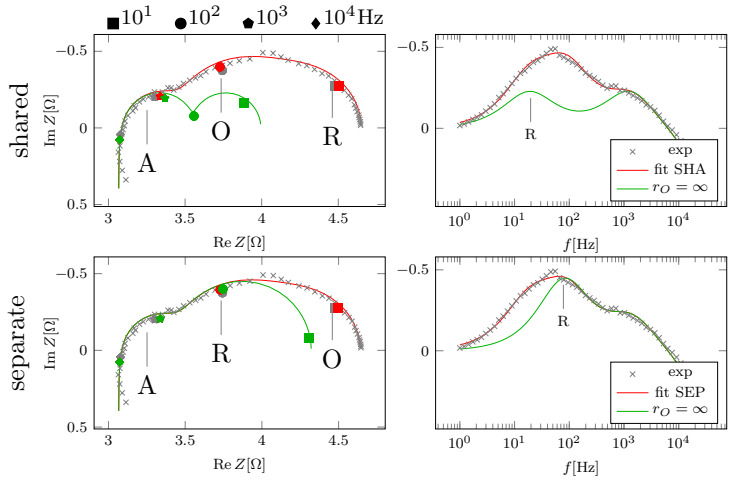


Figure 4: The $\mathrm{SHA}$model and $\mathrm{SEP}$model were fitted to EIS data at 800 °C and $60$% content of oxygen. Both models show three peaks in imaginary Bode diagrams (right) and provide an excellent agreement with measurement. However, there is a fundamental difference in peak-to-reaction relation. Green line shows the difference in case of equilibrated oxygen adsorption **O**, the peak belonging to the reaction **O** disappears and reveals the **R**-peak in the different frequency ranges.

as ids ls-SEP and ls-SHA, respectively. A decent agreement between simulated and experimental data is achieved in each case. As indicated in Table 3, the SHA scenario renders the oxygen adsorption $\mathbf{O}$ in the middle frequency range and the electron-transfer reaction $\mathbf{R}$ in the low frequency range unlike the SEP scenario. Since the oxygen adsorption is considered to be the slowest part of the reaction mechanism [8], the SEP scenario seems to provide a more realistic model of TPB. Moreover, the two possible surface site models have only marginal influence on CV results. Since no further apparent qualitative advantage of $\mathrm{SHA}$model was found, the rest of the study is focused on the $\mathrm{SEP}$scenario.

## 4.2 Discerning EXP and LoMA kinetics

Following (12g), this section showcases three kinetics scenarios: EXP kinetics, LoMA kinetics with $\zeta = 0$ and LoMA kinetics with $\zeta = 0.8$. The fits of the three cases are shown in Figure 5. The values of the parameters are listed in Table 2 as k-EXP, k-LoMA and k-LoMA-z, respectively.

The simulated impedance spectra in the EXP case can fit the measurement for a particular oxygen concentration. The simulation with the same parameters but a different oxygen concentration yields basically indistinguishable spectrum. This is in a strong disagreement with the experimental results.

The fit of the LoMA kinetics with $\zeta = 0$ provides a better agreement with the impedance data then the EXP case did.

Moreover, the simulated impedance spectra are in this case sensitive to different oxygen concentrations and this sensitivity resembles the experimental observation. The cyclic voltammetry indicates existence of limiting currents for the reduction as well as the oxidation reaction which are not observed in the experimental data.

The last fit is the LoMA kinetics with $\zeta = 0.8$. Non-zero value of the LSM charge distribution parameter allows for a fit which delays the onset of the limiting currents and preserves the qualitative behavior of the impedance spectra. Therefore, we pick the LoMA kinetics for the further investigation. The LSM charge distribution parameter $\zeta$ will be treated as a second fitting parameter along with $\nu^{\#}$.

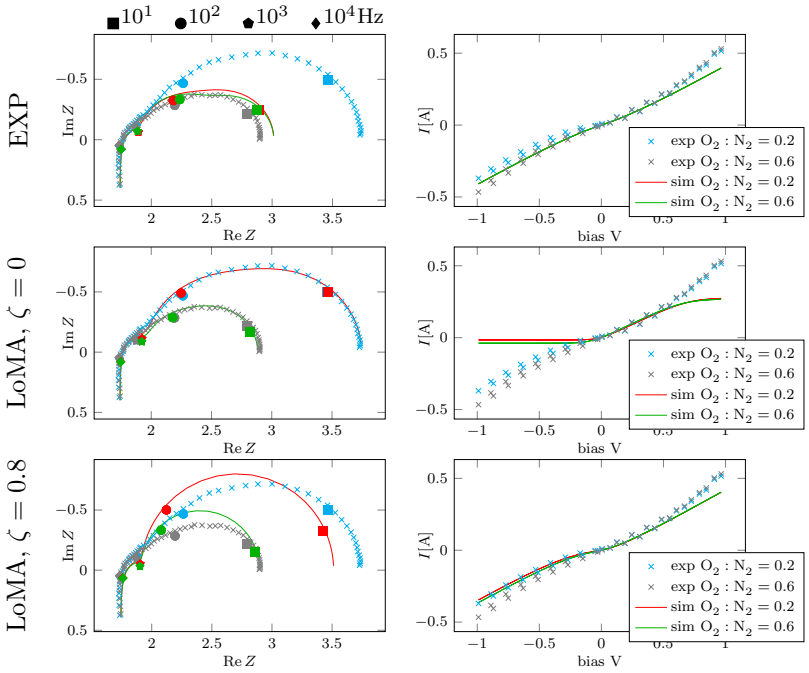


Figure 5: The presented experimental data are for 800 °C and 20 % and 60 % of oxygen:nitrogen ratio. The EXP kinetics (top row) fits well impedance and CV well for $O_2$ concentration. It does not follow the experimental trend for the other one. The LoMA kinetics with $\zeta = 0$ is unlike the previous case sensitive to the $O_2$ concentration similarly as the experimental observation. Nevertheless, it enters a plateau-like behavior for higher biases. The LoMA kinetics with $\zeta = 0.8$ retains the sensitivity to the $O_2$ concentration and at the same time captures CV sets on for higher bias.

# 5 Fit of the temperature dependent data

The model with the separated lattice sites SEP and the LoMA kinetics was selected for the evaluation of the temperature dependent data. The assumed temperature dependence of the model parameters is listed in Table 4.

Table 4: Temperature dependence of the fitted model parameters.

| parameter | temperature dependence |
|---|---|
| $\zeta$ | constant |
| $S^{\mathrm{A}}, S^{\mathrm{O}}, S^{\mathrm{R}}$ | constant |
| $C_{\mathrm{O}}, C_{\mathrm{O}^{2-}}$ | constant |
| $\Delta G^{\mathrm{A}}, \Delta G^{\mathrm{O}}, \Delta G^{\mathrm{R}}$ | linear |
| $\nu^{\#}$ | quadratic |
| $\bar{r}_0^{\mathrm{A}}, \bar{r}_0^{\mathrm{O}}, \bar{r}_0^{\mathrm{R}}$ | exponential |

Firstly, the fitting procedure was applied to obtain separate fits of EIS and CV at 700 °C and 750 °C and thus ballpark estimates of the fitted parameters and the temperature trends. The spectra for the two chosen temperatures exhibit three pronounced arcs which the fitting procedure failed to capture if initiated with the higher temperature spectra. The estimates of the parameter values and of the trends were used as initial values of the global temperature search through parametric space.

The model was fitted to the experimental dataset of EIS and CVs for 700 °C, 750 °C and 850 °C and 20 % and 60 % of $O_2$ atmosphere. The following choices of the EIS:CV weights were investigated: EIS-preferring 1:0 and EIS-CV-neutral 1:1.3. The neutral weights were chosen so that the cyclic voltammograms do not exhibit the limiting currents but the impedance spectra correlate with the experiment. The resulting fits of the experimental data are shown in Figures 6 and 7. The resulting temperature dependencies of the model parameters are shown in Figure 8. The values of the temperature independent parameters are listed in Table 5.

The fits of the data agree that the parameter $\nu^{\#}$ decreases with the temperature which means that number of mobile oxide ions in the bulk of YSZ increases with the temperature. The temperature trends of the reactions rates $\bar{r}_0^{\mathrm{X}}$ are in a good mutual agreement. This also holds for their values but the oxygen adsorption current exchange density $\bar{r}_0^{\mathrm{O}}$. At 850 °C is the EIS-preferring case value of $\bar{r}_0^{\mathrm{O}}$ approximately two orders of magnitude smaller than its value in the EIS-CV-neutral case. Albeit the trends of the reference reaction Gibbs energies $\Delta\bar{G}^{\mathrm{A}}$ and $\Delta\bar{G}^{\mathrm{R}}$ of the two fits do not agree, their absolute values are fairly close. The relative densities of the active surface lattice sites $C_{\mathrm{O}^{2-}}$ and $C_{\mathrm{O}}$, see Equation (10) and Table 5, are larger for the EIS-CV-neutral fit.

Table 5: Temperature-constant model parameters.

| EIS:CV weights | $\zeta$ | $S^{\mathrm{A}}$ | $S^{\mathrm{R}}$ | $S^{\mathrm{O}}$ | $C_{\mathrm{O}^{2-}}$ | $C_{\mathrm{O}}$ |
|---|---|---|---|---|---|---|
| 1:0 | 0.88 | 0.48 | 2.01 | 1.00 | 0.38 | 4.116 |
| 1:1.3 | 0.88 | 0.48 | 2.01 | 1.00 | 0.878 | 30.591 |

The forward and backward rates of the reactions are defined as

$$\bar{k}_f^X(T) = \bar{r}_0^{\mathrm{X}}(T)\exp\left(-S^X\frac{\Delta\bar{G}^{\mathrm{X}}}{2\bar{T}}\right), \tag{37}$$

$$\bar{k}_b^X(T) = \bar{r}_0^{\mathrm{X}}(T)\exp\left(S^X\frac{\Delta\bar{G}^{\mathrm{X}}}{2\bar{T}}\right), \tag{38}$$

and shown in Figure 9. The oxide adsorption reaction **A** turned out be the oxidation RLS of the EIS-CV-neutral fit. It is also the reduction RLS for this fit up to 780 °C where a transition to the electron-transfer reaction **R** occurs. The electron-transfer reaction **R** is the reduction RLS for the EIS-preferring fit up to 800 °C where the oxygen adsorption reaction **O** becomes the RLS. The oxygen adsorption reaction **A** is the oxidation RLS for the EIS-preferring fit.

# 6 Discussion

Mass-action kinetics based models assuming an ideal lattice gas with shared sites can be found in DFT studies of the surface chemistry of YSZ, see e.g. [4] or [16]. The presented model tests the difference between the shared and separate surface lattice sites models. The shared sites scenario renders the electron transfer reaction $\mathbf{R}^{\mathrm{SEP}}$ and the oxygen adsorption $\mathbf{O}$ into the low and mid frequency ranges of the impedance spectra, respectively. This situation is is not observed in the experimental results presented here nor in literature [17]. It would be interesting to verify this hypothesis in the realm of DFT.

Although the adopted model of the TPB does not seem to allow for the distinction between 2PB and 3PB pathways, comparison of the EIS-preferring and EIS-CV-neutral fits can be interpreted otherwise.

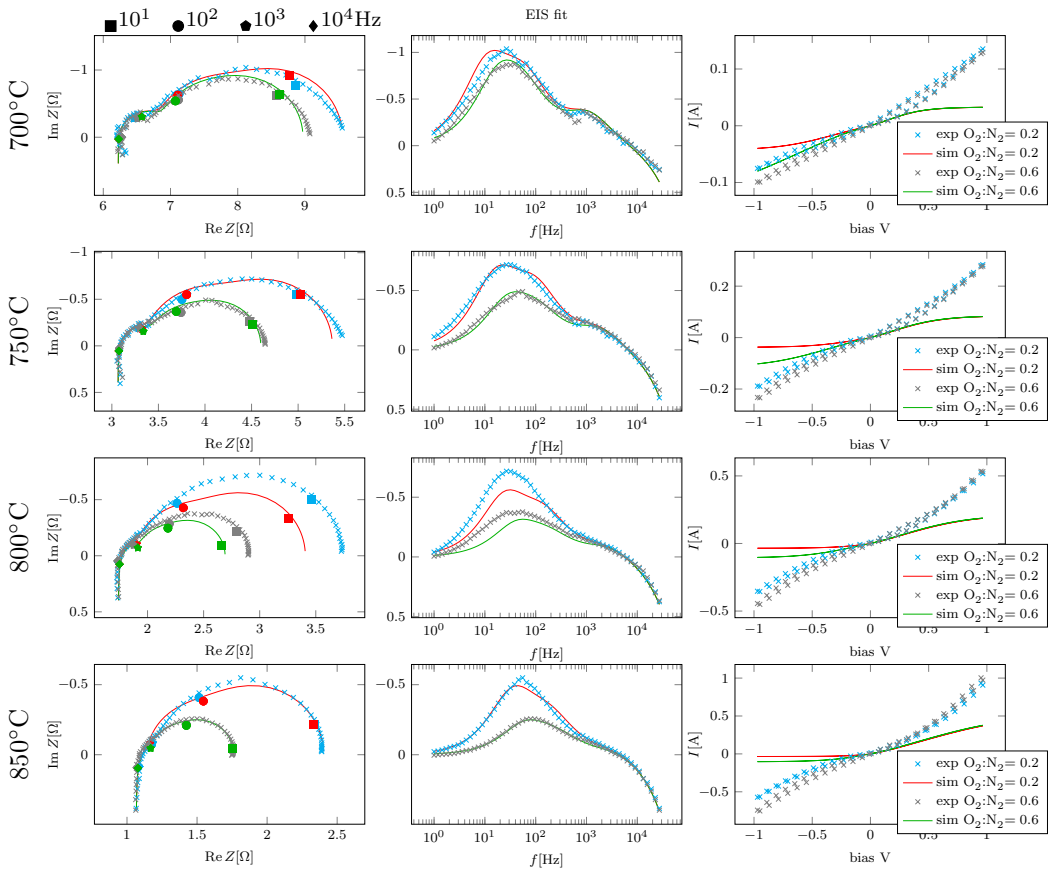


Figure 6: Fit of the model using only the impedance data, i.e. fit weights EIS:CV $1{:}0$, for 700 °C, 750 °C and 850 °C and 0.2 and 0.6 $O_2$:$N_2$ ratios at ambient pressure. The spectra measured at 800 °C are not fitted. The limiting current in the negative bias is due to the oxygen adsorption insufficiency.

The EIS-preferring fit shows a good agreement in the vicinity of the OCV but exhibits a limiting current density around $-0.2\,\mathrm{V}$ overpotential. The respective values of $C_{\mathrm{O}}$ and $C_{\mathrm{O}^{2-}}$ correspond to a limited extent of the TPB and are thus consistent with the 3PB pathway [8]. The EIS-CV-neutral fit overcomes the limiting currents due to increasing the forward and backward rate coefficients of the oxygen adsorption reaction by orders of magnitude, see Figure 9 At the same time, the forward and backward rate coefficients of the electron-transfer and the oxygen adsorption reactions remain of the same order of magnitude. Since the current exchange densities $\bar{r}_0^{\mathrm{X}}$ are not scaled w.r.t. $C_{\mathrm{O}}$ and $C_{\mathrm{O}^{2-}}$, the excessive values of the forward and backward oxygen adsorption reaction rates suggest that a disproportionally large surface is required for the adsorption and hence a different, possibly 2PB pathway, is exhibited [7]. The values of $C_{\mathrm{O}}$ and $C_{\mathrm{O}^{2-}}$ cannot be attributed to the 2PB pathway, since the cyclic voltammetry operates very close to a steady state regime and it is thus virtually independent of the coefficients in front of the terms with time derivative, see Equation (10).

Since the EIS-preferring fit accurately simulates the measurements around the OCV, the derived reaction rates carry a relevant information about the chemistry of the YSZ|LSM|$O_2$ interface. This does not hold for the EIS-CV-neutral fit. In order to establish an accurate EIS-CV-neutral fit with the current domain geometry–1D electrolyte endowed with a point TPB–it would suffice to introduce a parallel electron-transfer reaction pathway. The presented model exhibits in total four peaks in the impedance spectrum, see Figure 10. Each peak represents, in the context of the fitting, a degree of freedom. The GHz-frequency peak is expended to fit the bulk YSZ conductivity. The three remaining peaks–degrees of freedom–are used to fit the peaks of the experimental spectrum. Nevertheless, the benefit of the re-

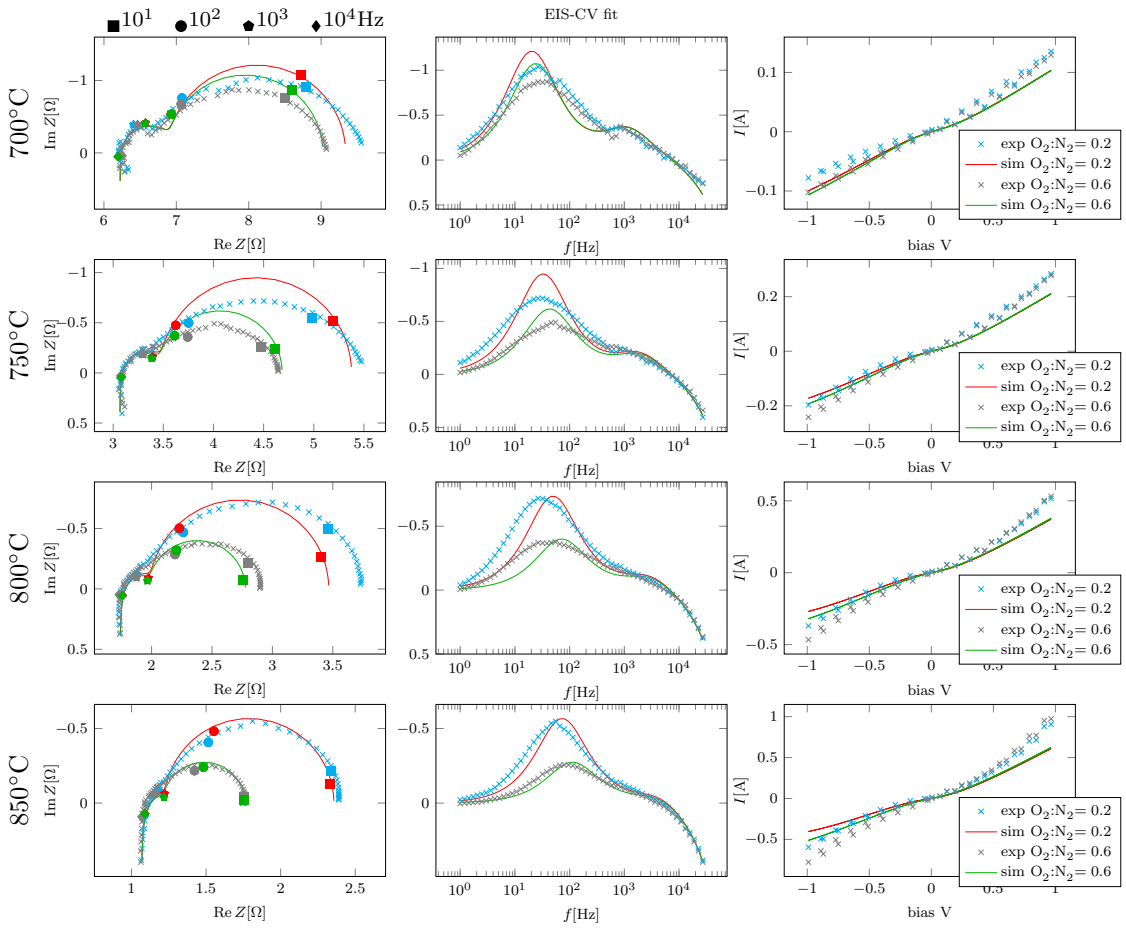


Figure 7: Fit of the model using the impedance and cyclic voltammetry data, i.e. fit weights EIS:CV $1{:}1.8$, for 700 °C, 750 °C and 850 °C and 0.2 and 0.6 $O_2$:$N_2$ ratios at ambient pressure. The spectra measured at 800 °C are not fitted.

action mechanism extension is questionable, since it would bring additional fitting parameters without the ability distinguish the reaction pathways geometrically.

# 7 Conclusion

The generalized Poisson-Nernst-Planck model of YSZ allows to resolve the IR drop in the electrolyte bulk as well as the spatial profile of the electrostatic potential in the electrolyte near the working electrode interface, see Figure 3. This allows for the estimation of the electrode potential of the working electrode using an LSM charge distribution parameters $\zeta$. The model attempts to capture the actual drop of the electrostatic potential across the double layer. This allows a for a more accurate representation of the potential difference driving the reaction. Finally, it permits to express the unknown chemical potential of the electrons at the TPB as a sum of the chemical potential of the electrons in the bulk LSM and the change of the electrostatic potential between the bulk LSM and the TPB.

The separate lattices sites model $\mathrm{SEP}$ renders the oxygen adsorption in the low frequency part of the spectrum in accordance with the experiments unlike the shared lattice sites model $\mathrm{SHA}$. Law of mass action kinetics is essential to capture the pressure sensitivity of the impedance spectra observed in the experiments. The combined fitting of the electrochemical impedance spectroscopy and cyclic voltam-

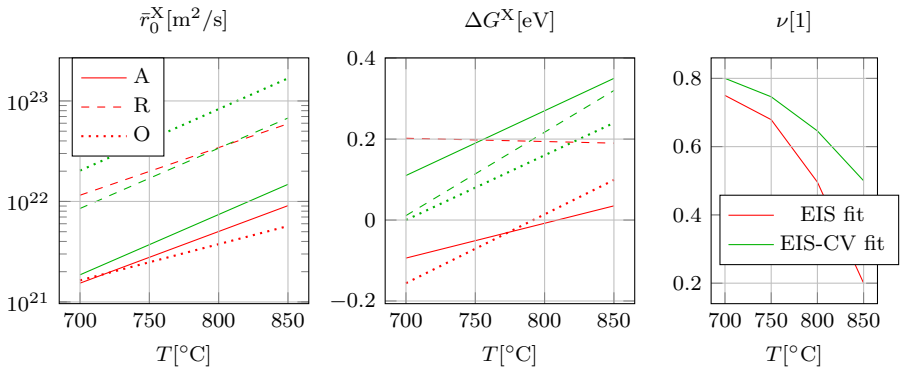


Figure 8: Temperature dependent model parameters. The red and green color indicates the EIS-preferring and EIS-CV-neutral fits, respectively. The solid, dashed and dotted lines indicate the oxide adsorption reaction, electron-transfer reaction and the oxygen adsorption reaction, respectively.

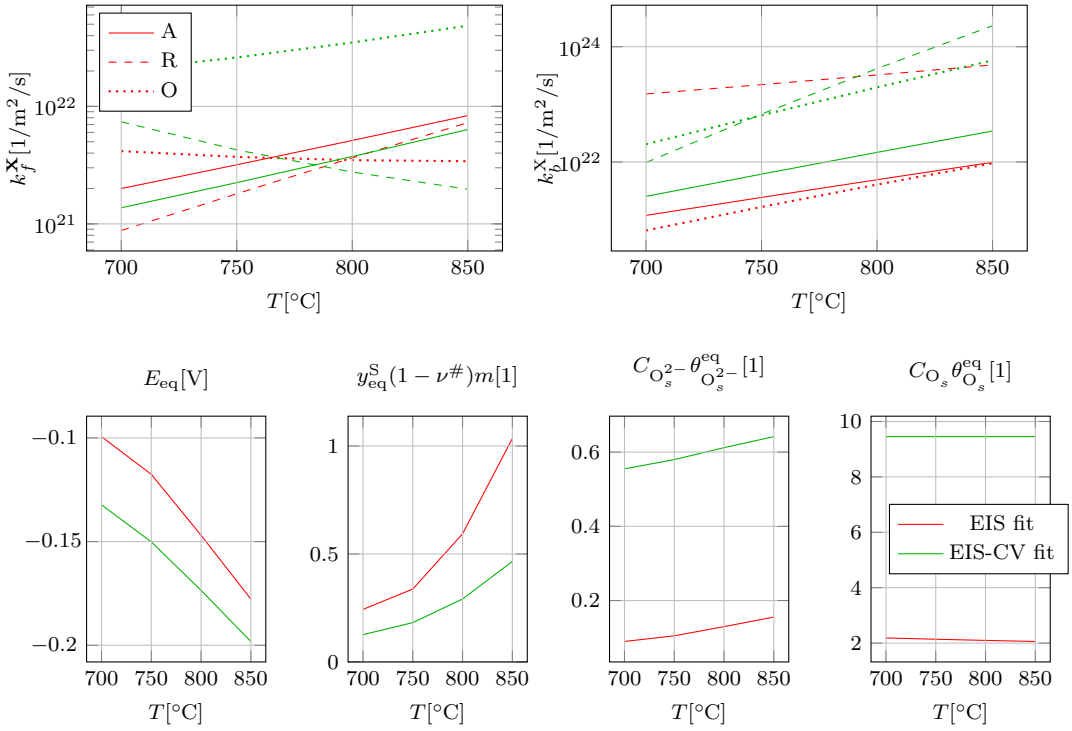


Figure 9: Temperature dependence of the forward (ORR regime, negative overvoltage) and backward (OER regime, positive overvoltage) reaction rates shows the rate limiting steps (top row). Temperature dependence of the equilibrium values of the working electrode potential $E^{\mathrm{eq}}$ and the equilibrium coverages of the TPB species which are expressed relatively to the number of volume cation lattice sites, in the case of $y$, and surface cation lattice sites, in the case of $\theta$ (bottom row).

metry experiments has brought an additional insight into the electrode kinetic mechanism despite the loss of the fit accuracy. Two particular choices of the fitting weights were considered: the EIS-preferring fit and EIS-CV-neutral fits. The EIS-preferring fit, relying exclusively on the EIS data, has identified the 3PB oxygen reduction reaction pathway but exhibited limiting currents not observed in the experimental data. The EIS-CV-neutral fit, reflecting also the cyclic voltammetry, has captured the experimentally observed trend of the cyclic voltammetry and thus unveiled the transition to a 2PB pathway while misestimating the total polarization resistance. Although the model is isothermal and does not cover

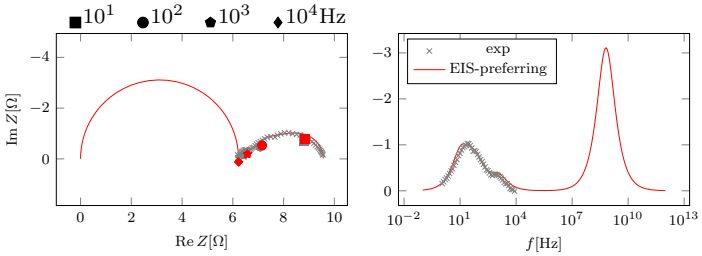


Figure 10: Frequency extrapolation of experimental data at 700 °C and 20 % oxygen using EIS-preferring fit presented in section (5). The extended frequency range is $10^{-1}$ - $10^{13}$Hz. Inductance is set to $L = 0$ H. Simulation slows three arcs within the experimental range and the fourth arc connected with electrolyte bulk which is commonly interpreted as ohmic resistance.

electron and oxide ion transport in LSM, it exhibits a good agreement across a significant range of temperatures and oxygen/nitrogen ratios in the vicinity of the OCV. Given its thermodynamically consistent formulation, the model can be straightforwardly extended to a nonisothermal setting which would permit to evaluate the energy dissipation and entropy production regarding specific processes such as bulk transport or individual steps of reaction mechanism.

The relation of the electrochemical potential of the electrons at TPB and in the LSM bulk was crucial to establish the combined fitting. An extended model including electron an ion transport in a spatially resolved LSM compartment similarly to [18] would allow to gain more precise insight into the LSM part of the space charge layer and thus will be the subject of future research.

## References

[1] Johan E. ten Elshof, Mark G. H. M. Hendriks, Henny J. M. Bouwmeester, and Henk Verweij. The near-surface defect structure of yttria-stabilised zirconia determined by measurement of the differential capacity. *Journal of Materials Chemistry*, 11(10):2564–2571, 2001.

[2] M. M. Kuklja, E. A. Kotomin, R. Merkle, Yu. A. Mastrikov, and J. Maier. Combined theoretical and experimental analysis of processes determining cathode performance in solid oxide fuel cells. *Physical Chemistry Chemical Physics*, 15(15):5443, 2013.

[3] Y Ji, J Kilner, and M Carolan. Electrical properties and oxygen diffusion in yttria-stabilised zirconia (YSZ)– –LaSrMnO (lsm) composites. *Solid State Ionics*, 176(9–10):937–943, Mar 2005.

[4] Yuri A. Mastrikov, Rotraut Merkle, Eugene Heifets, Eugene A. Kotomin, and Joachim Maier. Pathways for oxygen incorporation in mixed conducting perovskites: A dft-based mechanistic analysis for (La, Sr)$MnO_{3-\delta}$. *The Journal of Physical Chemistry C*, 114(7):3017–3027, Feb 2010.

[5] J. Fleig, Rotraut Merkle, and Joachim Maier. The p(o2) dependence of oxygen surface coverage and exchange current density of mixed conducting oxide electrodes: model considerations. *Physical Chemistry Chemical Physics*, 9(21):2713, 2007.

[6] Mingyang Gong, Randall S. Gemmen, and Xingbo Liu. Modeling of oxygen reduction mechanism for 3pb and 2pb pathways at solid oxide fuel cell cathode from multi-step charge transfer. *Journal of Power Sources*, 201:204–218, Mar 2012.

[7] Mingyang Gong, Randall S. Gemmen, David S. Mebane, Kirk Gerdes, and Xingbo Liu. Simulation of surface-potential driven orr kinetics on sofc cathode with parallel reaction pathways. *Journal of The Electrochemical Society*, 161(3):F344–F353, 2014.

[8] A. Bertei, M.P. Carpanese, D. Clematis, A. Barbucci, M.Z. Bazant, and C. Nicolella. Understanding the electrochemical behaviour of lsm-based sofc cathodes. part ii - mechanistic modelling and physically-based interpretation. *Solid State Ionics*, 303:181–190, May 2017.

[9] Tao Yang, Jian Liu, Harry O. Finklea, Harry Abernathy, and Gregory A Hackett. Multi-physics simulation of SOFC button cell with multi-step charge transfer model in composite LSM/YSZ cathode. *ECS Transactions*, 78(1):2699–2709, May 2017.

[10] A. Banerjee and O. Deutschmann. Elementary kinetics of the oxygen reduction reaction on lsm-ysz composite cathodes. *Journal of Catalysis*, 346:30–49, Feb 2017.

[11] Tao Yang, Sezer Hayri, Ismail Celik, Harry Finklea, and Kirk Gerdes. Prediction of sofc performance with or without experiments: A study on minimum requirements for experimental data. *International Journal of Electrochemical Science*, page 6801–6828, Jul 2017.

[12] Petr Vágner, Clemens Guhlke, Vojtěch Miloš, Rüdiger Müller, and Jürgen Fuhrmann. A continuum model for yttria-stabilized zirconia incorporating triple phase boundary, lattice structure and immobile oxide ions. *Journal of Solid State Electrochemistry*, 23(10):2907–2926, Oct 2019.

[13] J. Fuhrmann. VoronoiFVM.jl - Solver for coupled nonlinear partial differential equations based on the Voronoi finite volume method. `https://github.com/j-fu/VoronoiFVM.jl`, 2019.

[14] Michael A. Danzer. Generalized distribution of relaxation times analysis for the characterization of impedance spectra. *Batteries*, 5(3):53, Jul 2019.

[15] matthieugomez. LeastSquaresOptim.jl - Solver for non linear least squares optimization problems. `https://github.com/matthieugomez/LeastSquaresOptim.jl`, 2019.

[16] Salai Cheettu Ammal and Andreas Heyden. Combined dft and microkinetic modeling study of hydrogen oxidation at the ni/ysz anode of solid oxide fuel cells. *The Journal of Physical Chemistry Letters*, 3(19):2767–2772, Oct 2012.

[17] M.P. Carpanese, D. Clematis, A. Bertei, A. Giuliano, A. Sanson, E. Mercadelli, C. Nicolella, and A. Barbucci. Understanding the electrochemical behaviour of lsm-based sofc cathodes. part i — experimental and electrochemical. *Solid State Ionics*, 301:106–115, Mar 2017.

[18] D Abdel, P Vágner, J Fuhrmann, and P Farrell. Modelling charge transport in perovskite solar cells: Potential-based and limiting ion vacancy depletion. page 26, 2020.